The University of Manchester Research

On the Mechanism of Turbulent Heat Transfer in Composite Porous-Fluid Systems with Finite Length Porous Blocks: Effect of Porosity and Reynolds number

Document Version
Accepted author manuscript

Link to publication record in Manchester Research Explorer

Citation for published version (APA):
Jadidi, M., Khalili Param, H., & Mahmoudi Larimi, Y. (Accepted/In press). On the Mechanism of Turbulent Heat Transfer in Composite Porous-Fluid Systems with Finite Length Porous Blocks: Effect of Porosity and Reynolds number. *International Journal of Heat and Mass Transfer*.

Published in:
International Journal of Heat and Mass Transfer

Citing this paper
Please note that where the full-text provided on Manchester Research Explorer is the Author Accepted Manuscript or Proof version this may differ from the final Published version. If citing, it is advised that you check and use the publisher's definitive version.

General rights
Copyright and moral rights for the publications made accessible in the Research Explorer are retained by the authors and/or other copyright owners and it is a condition of accessing publications that users recognise and abide by the legal requirements associated with these rights.

Takedown policy
If you believe that this document breaches copyright please refer to the University of Manchester's Takedown Procedures [http://man.ac.uk/04Y6Bo] or contact uml.scholarlycommunications@manchester.ac.uk providing relevant details, so we can investigate your claim.

OPEN ACCESS

Download date:04. Mar. 2023

On the Mechanism of Turbulent Heat Transfer in Composite Porous-Fluid Systems with Finite Length Porous Blocks: Effect of Porosity and Reynolds number

Mohammad Jadidi[1], Hanieh Khalili Param[2], Yasser Mahmoudi[1*]

[1]Department of Mechanical, Aerospace and Civil Engineering (MACE), University of Manchester, M13 9PL, UK
[2]Department of Mechanical, Automotive and Material Engineering (MAME), University of Windsor, N9B 3P4, Canada

[*]Corresponding author: yasser.mahmoudi@manchester.ac.uk

Abstract

The majority of literature studies on composite porous-fluid systems involve fully-developed porous channel flows where the porous media covers the whole length of the channel. These studies utilized periodic boundary conditions at the inlet and outlet. In these systems, the stagnation at the frontal face of the porous block, turbulent separation bubble over the porous-fluid interface, and flow leakage from the porous to non-porous regions do not exist. The existence of these flow features in the case of a finite porous block immersed in a channel flow modifies turbulent interactions across the porous-fluid interface. In contrast to the previous studies, this paper investigates the flow and thermal characteristics of turbulent channel flow containing a porous block with a finite length. To this end, pore-scale large eddy simulations are performed in composite porous-fluid systems with two porosities (53% and 91%) at three Reynolds numbers of 3600, 7200, and 14400. Flow visualization shows that two distinct regions are formed over the interface in low-porosity cases, in contrast to high-porosity cases: Region#1 near the leading edge with organised hairpin structures and high flow leakage; Region#2 away from the leading edge with unorganised hairpin structures and lower flow leakage. In region#1, maximum turbulent fluctuations occur far away from the interface while they approach the interface in region#2. The results showed that by increasing either the Reynolds number or porous length, the location of maximum turbulence statistics approaches the interface. This observation supports earlier findings for fully-developed porous channel flows which are only valid in region#2. Whereas, with a low Reynolds number or a short porous length, the turbulent statistics peak far from the interface, consistent with the observations in region#1. Besides, it was found that increasing the porosity and Reynolds number reduces the flow leakage (from the porous region to the non-porous region) up to 50% and 10%, respectively, which in turn disrupts the patterns of contour-rotating vortex pairs and hairpin structures over the interface. It is further found that for a fixed Reynolds number, the overall Nusselt number for the high-porosity case is 2.6 times higher than that of the low-porosity case. The pressure drop for the low-porosity cases is 1.8 times more than that for the high-porosity cases.

Keywords

Turbulent porous flow; Momentum and energy exchange; Flow leakage; Finite porous block; Pore-scale large eddy simulations; Nusselt number; Pressure drop.

1 Nomenclature

variable	Meaning	Unit
A_s	Surface area of the pore element	m^2
dA	Differential surface area on the pore element	m^2
D	Distance between the centres of two consecutive pore elements	m
$d_{\Phi=53\%}$	Diameter of pore elements for low-porosity cases with porosity equal to 53%	m
$d_{\Phi=91\%}$	Diameter of pore elements for high-porosity cases with porosity equal to 91%	m
h	Height of the porous block	m
H	Channel height	m
k	Turbulent kinetic energy	m^2/s^2
k_f	Thermal conductivity of the working fluid	W/m.K
L	Length of the porous block	m
p	Pressure	Pa
q_{wall}	Heat flux on the wall	W/m^2
Q	Second invariant of velocity gradient tensor	$1/s^2$
Q_{in}	Flow rate that enters the porous block from the frontal face	m^3/s
Q_{lX}	Flow rate that leaks from the X-percentage of the porous-fluid interface	m^3/s
R_{vv}	Auto-correlation of vertical velocity fluctuations (v')	–
$R_{A,B}$	Temporal cross-correlation of vertical velocity fluctuations for arbitrary points A and B	–
$Re = UH/\upsilon$	Reynolds number based on the inlet bulk velocity and channel height	–
$Re_{d,\Phi} = Ud_{\Phi}/\upsilon$	Reynolds number based on the inlet bulk velocity and pore element's diameter	
$Re_h = Uh/\upsilon$	Reynolds number based on the inlet bulk velocity and porous block height	
$\bar{S}_{ij}$	Resolved strain rate tensor	1/s
t	Time	s
$t^* = t \times U/D$	Non-dimensional time unit	–
T	Temperature	K
Δt	Time step	s
u'_i	Velocity fluctuation in i[th] direction, $u'_i = \bar{u}_i - < \bar{u}_i >$	m/s
$u^{*\prime} = u'/U$	Non-dimensional streamwise velocity fluctuation	–
u	Streamwise velocity component	m/s
U	Inlet bulk velocity	m/s
v	Vertical velocity component	m/s
X	Streamwise direction	m
Y	Vertical direction	m
$\widetilde{\Delta Y}$	Mean cell size in the vertical direction	m
Z	Spanwise (Lateral) direction	m
Symbol		
β	Angle of the connecting line between the hairpin's leg and head with regard to the horizontal direction	degree
Υ	Pearson linear correlation coefficient	–
Δ	Filter width	m
$\Theta = \dfrac{T - T_{inlet}}{T_{wall} - T_{inlet}}$	Non-dimensional temperature	–
λ	Integral length scale	m
υ	Molecular kinematic viscosity	m^2/s
υ_{SGS}	Sub-grid scale eddy viscosity	m^2/s
ρ	Density	kg/m^3
$\sigma_u = u'/u_{RMS}$	Non-dimensional streamwise velocity fluctuation	–
$\sigma_v = v'/v_{RMS}$	Non-dimensional vertical velocity fluctuation	–
τ_{ij}	Sub-grid scale (SGS) turbulent stress tensor	m^2/s^2
Φ	Porosity	–

Ω_{ij}	Rotation rate tensor	1/s
$\langle\ \rangle$	Time-averaging operator	−
Subscript		
loc	local	
Num	Numerical	
res	Resolved	
RMS	Root mean square	
s	Surface of pore element	
SGS	Sub-grid scale	
Superscript		
$\overline{}$	Filtration (top hat filter)	
$'$	Fluctuation	
Abbreviation		
$AR = L/h$	Aspect ratio, i.e., ratio of the porous block's length to its height	−
$BR = h/H$	Blockage ratio, i.e., ratio of the porous block's height to channel height	−
CFL	Courant–Friedrichs–Lewy number	−
CRVP	Counter-rotating vortex pair	−
JPDF	Joint probability density function	−
K-H	Kelvin-Helmholtz	−
LES	Large Eddy Simulations	−
$LR = L/D$	Length ratio, i.e., ratio of the porous block's length to distance between the centres of two consecutive pore elements	−
Nu	Nusselt number	−
Re	Reynolds number	−
TSB	Turbulent separation bubble	−
TKE	Turbulent kinetic energy	m^2/s^2

1 Introduction

An extensive range of man-made technologies and natural phenomenon involves flow and heat transfer over composite porous-fluid systems, which consist of a fluid-saturated porous medium and a flow passing over it. Examples are: Flows in fuel cells [1-3], packed bed energy storage systems [4-8], battery thermal management [9-11], cooling in the gas turbine [12-14], metal foam heat sinks for electronic cooling [15, 16]. In these applications, the porous block allows mass, momentum, and energy exchange between porous and non-porous regions. Despite extensive analytical [17, 18], numerical [19-22], and experimental [16, 23-25] research in the literature to explore the turbulent fluid flow and heat transfer over the composite porous-fluid systems, there are several open questions remained unanswered yet. The major challenge is to find how the flow in the porous region interacts with the non-porous region and consequently, its impacts on the characteristics of flow and thermal fields in the system.

At high Reynolds numbers ($Re_{d,\Phi} > 750$), turbulent flow is observed in porous media [3]. This is determined by the pore Reynolds number ($Re_{d,\Phi} = Ud_{\Phi}/\upsilon$), which is calculated using the mean average velocity (U), the mean particle diameter (d_{Φ}), and the kinematic viscosity of the fluid (υ). When $Re_{d,\Phi} >$ 25, convection is a major factor, with steady vortices potentially forming, and when $Re_{d,\Phi} < 750$, the flow regime is unsteady laminar, where transitional effects and periodic vortices are present [3]. Literature has extensively explored turbulent interactions across the interface between the porous and non-porous regions (porous-fluid interface) [19, 26-28]. However, the majority of these studies involve fully-developed porous channel flows, where the whole length of the bottom wall is covered with the porous medium [19, 21, 24, 25]. In these studies, periodic boundary conditions are applied at the inlet and outlet. Therefore, the stagnation at the frontal face of the porous block, turbulent separation bubble (TSB) over the porous-fluid interface, the wake region after the porous block, and the flow leakage from the porous into non-porous regions have not been observed. A composite porous-fluid system with a finite porous block immersed in a channel flow exhibits different turbulent interactions across the interface compared to a fully-developed porous channel flow. For the latter one, a sudden change in the turbulence statistics is detected near the porous-fluid interface [19, 23-25, 29]. In contrast, for the former one (finite length porous block), the sudden change in the turbulence statistics occurs away from the interface [30, 31]. This means that in the case of a finite porous block, the earlier findings in the literature [24, 25, 28, 29, 32] are not valid over the entire porous length. Therefore, the momentum and energy exchange for the fully-developed porous channel flow cannot be generalized for the cases with a finite porous block immersed in a turbulent channel flow.

Only a few experiments have addressed the turbulence interactions at the porous-fluid interface for the cases with a finite porous block immersed in a turbulent channel flow [33-36]. Anuar et al. [33, 34] performed experimental studies on a channel partially filled with metal foam blocks with different porosities and inlet velocities. According to the results, the portion of the fluid entering the porous region passes through the porous structure and enters the non-porous region (flow leakage). This phenomenon was more pronounced for low-pore density foams, while high-pore density foams showed more restrictions for pushing the fluid from the porous region into the non-porous region. In another study by Anuar et al. [36], the flow leakage was investigated experimentally by the particle transport and deposition processes within turbulent channels partially filled with metal foams. Foam arrangement and blockage ratios were reported as influential parameters for the flow leakage and deposition of particles [36].

Recent evidence witnesses that high-fidelity pore-scale numerical simulations enable microscopic visualization and analysis of momentum and energy exchange in porous media, which are hardly achievable in experiments with confined and tortuous spaces [21, 37-39]. Recently, Siavashi et al. [40-42] performed a series of pore-scale direct numerical simulations (DNS) of flow (Darcy and non-Darcy flows) and heat transfer in porous foams occupying the whole flow-pass area of the channel. In their studies, the effects of different parameters including pores numbers per inch (PPI), porosity, and permeability are examined within a wide range of Re_k (based on inlet velocity and permeability k). The results proved that reducing the porosity increases the flow complexity and consequently increases the pressure drop and heat transfer. Wang et al. [37] studied turbulence interactions between the boundary layer and porous media, using direct numerical simulation (DNS). Their results proved the profound impact of the porosity on the intensity, time scale, and spatial extent of top-down and bottom-up interactions across the porous-fluid interface. Chu et al. [21] explored turbulence transport across the interface at two Reynolds numbers ($Re \sim 3000$ and 6000 based on bulk inlet velocity and channel height) and two porosities (Φ = 50% and 80%), using the DNS approach. The results demonstrated that the turbulence transportation near the porous-fluid interface is strongly influenced by the porosity variations. Turbulent diffusion and pressure transportation is reported as energy sink and source, respectively, leading to turbulence transport into the porous region. Korba and Li [43] investigated the impacts of pore-scale and conjugate heat transfer on the convective heat transfer in porous media by the DNS approach. They indicated that the boundary layer thickness is determined by the pore element size. Also, it was reported that the Nusselt (Nu) number increases by decreasing the pore size.

Recently, Jadidi et al. [30, 31] utilized pore-scale large eddy simulation (LES) to investigate flow and heat transfer in a composite porous-fluid system with a finite-length porous block. The porous block's characteristics were as follows: BR = 0.5 (BR is blockage ratio which is the ratio of the porous height to the channel height); AR = 3.3 (AR is the aspect ratio defined as the ratio of the porous length to its height); LR = 10 (LR is the length ratio defined as the ratio of porous length to the pore element diameter). In contrast to fully-developed porous channel flows [24, 25, 28, 29, 32], Jadidi et al. [30, 31] showed a different pattern for the distribution of turbulent kinetic energy (TKE), turbulence production and consequently, turbulent heat flux above the interface due to the finite length of the porous block. They reported that the turbulent interactions between the porous and non-porous regions are mainly governed by the TSB and flow leakage.

According to the discussions above and previous findings of the current authors, there is a substantial gap in the literature for the momentum and energy exchange in composite porous-fluid systems with a finite porous block. In particular, the geometric properties of the porous medium (i.e., porous length and porosity) and the flow regime (i.e., Reynolds number) are expected to have a profound effect on the formation of the major physical phenomena in the porous-fluid systems. These main phenomena including Kelvin-Helmholtz instability, flow leakage, flow separation at the leading edge, and the downstream wake flow were found to play crucial roles in the exchange of the flow and thermal properties across the porous-fluid interface. The present work aims at filling the gap of the influence of the porosity and Re number on the mentioned flow features and consequently momentum and energy exchanges in composite porous-fluid systems with a finite porous length. To this end, comprehensive pore-scale large eddy simulations (LES) are performed for composite porous-fluid systems with finite lengths at different Re numbers and different porosities. The present study will answer the challenging questions about the validity of turbulence interactions over the interface associated with the earlier findings of the composite porous-fluid system modelled as a fully-developed porous channel flow with periodic boundary conditions.

2 Computational methodology

2.1 Geometry and boundary conditions

The computational geometry consists of a channel flow with the dimensions of $70D$, $6D$, and $4D$ in the X, Y, and Z directions, respectively. "D" is the distance between the centres of two consecutive pore elements. A porous bluff body characterized by BR = 0.5, AR = 6.6, and LR = 20 is mounted inside the channel at X/D = 0, as shown in **Figure 1**(a). Two different porous blocks containing cubic packed arrangements formed from spheres (pore element) with two different porosities, Φ = 53% (low porosity) and Φ = 91% (high porosity), are employed, as can be seen in **Figure 1**(b, c). An in-line arrangement is utilized to reduce the geometry complexity and simplify the computational domain. There are several pore-scale studies that used the in-line arrangement for presenting the porous block [21, 37]. Three different flow Reynolds (Re) numbers, 3600, 7200, and 14400 based on the inlet velocity (U) and the channel height (H) are considered for each porosity which led to a total number of six different case studies. The corresponding $Re_{d,\Phi}$ numbers based on the inlet bulk velocity and pore element's diameter are 600, 1200, and 2400 for low-porosity cases and 288, 576, and 1152 for high-porosity cases. In addition, the corresponding Re_h numbers based on the inlet bulk velocity and porous block height are 1800, 3600, and 7200 for both low- and high-porosity cases. At the inlet of the domain, constant velocity, and constant non-dimensional temperature (i.e., $\Theta = (T - T_{inlet})/(T_{wall} - T_{inlet}) = 0$) are applied. In addition, the no-slip boundary condition is utilized on the sphere walls, and top and bottom walls. A constant non-dimensional temperature (Θ = 1) is implemented on the sphere walls, while the bottom and top boundaries are adiabatic walls. For the side walls in the computational domain symmetry condition is utilized. The applied boundary conditions are displayed in **Figure 1**(a). **Figure 1**(d) depicts the topology of the generated mesh around the pore elements.

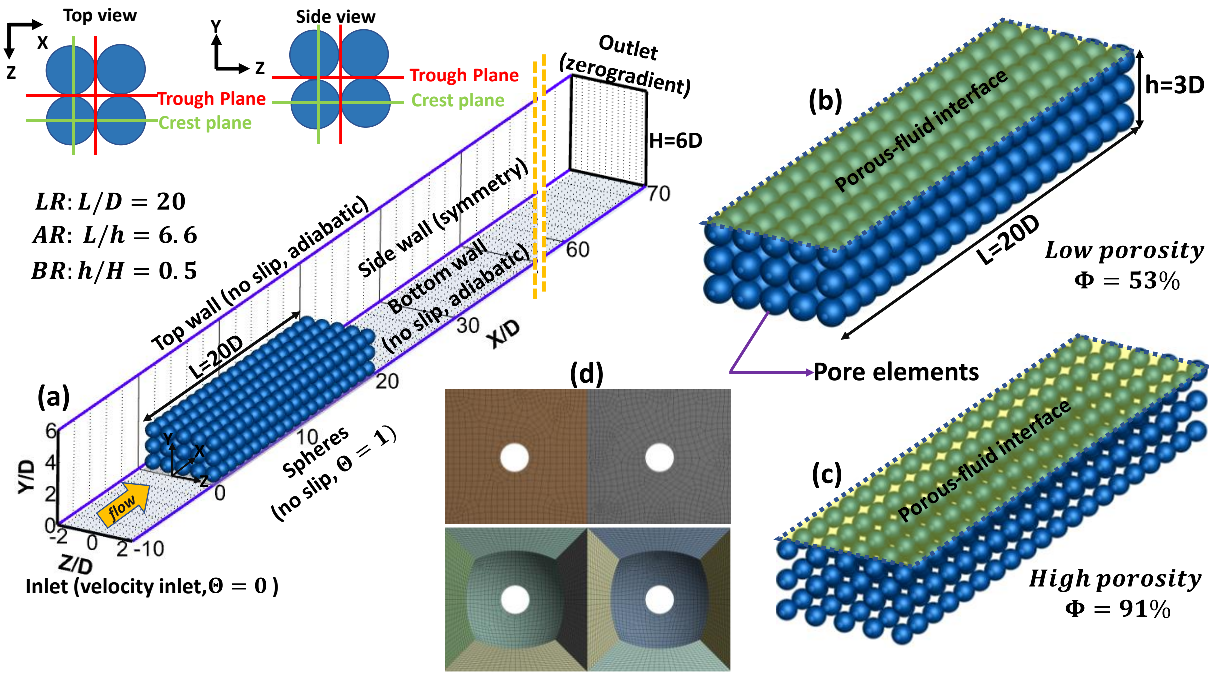

Figure 1 (a) Computational domain, boundary conditions, and porous block with cubic packed arrangement formed from spheres with the consecutive distance of D = 6mm distance; **(b)** Porous block with porosity of 53% and $d_{\Phi=53\%} = 1.0D$; **(c)** Porous block with porosity of 91% and $d_{\Phi=91\%} = 0.55D$; **(d)** Topology of the generated mesh around the spheres; Red and green lines: Illustration of two spanwise and streamwise locations for presenting results, the red line lies over the "trough plane" and the green line lies over the "crest plane".

The green and red lines on the top and side views in **Figure 1**(a) illustrate two streamwise/spanwise locations, namely: "crest plane" and "trough plane", where the LES results are extracted. For low-porosity cases, the bridge method is employed at the contact point of the spheres to overcome the problem of highly skewed mesh and consequently numerical errors of simulation [44]. The trough plane is located at the centre of the connecting bridges that connect the spheres in low-porosity cases. However, the crest plane crosses through the centres of the pore elements. A locally impermeable interface exists on the crest plane, preventing flow penetration there. Though, the porous and non-porous regions of the trough plane can exchange fluid thanks to the open (permeable) interface in the trough plane.

2.2 Numerical details

The governing equations for the incompressible flow of the present study are continuity, Navier-Stokes (momentum), and energy equations. Top-hat filtering is applied to the governing equations, resulting in the resolved LES equations as follows [45, 46]:

$$\frac{\partial \overline{u_i}}{\partial X_i} = 0 \tag{1}$$

$$\frac{\partial \overline{u_i}}{\partial t} + \frac{\partial}{\partial X_j}\left(\overline{u_i}\overline{u_j}\right) = -\frac{1}{\rho}\frac{\partial \bar{p}}{\partial X_i} + \frac{\partial}{\partial X_j}\left(\upsilon\frac{\partial \overline{u_i}}{\partial X_j} - \tau_{ij}\right) \tag{2}$$

$$\frac{\partial \overline{\mathrm{T}}}{\partial t} + \frac{\partial}{\partial X_j}\left(\overline{\mathrm{T}}\overline{u_j}\right) = \frac{\partial}{\partial X_j}\left(\left(\alpha + \alpha_{SGS}\right)\frac{\partial \overline{\mathrm{T}}}{\partial X_j}\right) \tag{3}$$

Here, $(\overline{...})$ refers to the filtration operation. Thus, $\overline{p}$, $\overline{u_i}$ and $\overline{T}$ represent the filtered pressure, velocity in i^{th} direction, and temperature, respectively. The solution of the Eqs. (1-3) illustrate the resolved scales which are energy-containing large scales in the flow field. The small scales that are removed by the filtering process show their impacts on the resolved flow field by an unknown turbulent stress tensor, called the sub-grid scale (SGS) tensor (τ_{ij}). The SGS stress (defined as $\tau_{ij} = \overline{u_i u_j} - \overline{u_i}\,\overline{u_j}$) is estimated by the following expression which is similar to the Boussinesq hypothesis.

$$\tau_{ij} - \frac{1}{3}\tau_{kk}\delta_{ij} = -2\upsilon_{SGS}\,\overline{S_{ij}} = -2C_{\tau}\,\Delta\,k_{SGS}^{1/2}\,\overline{S_{ij}} \tag{4}$$

In Eq. (4) υ_{SGS} is the sub-grid scale (SGS) turbulent viscosity which is modelled by localized dynamic k_{SGS}-equation model [47]. α_{SGS} in Eq. (3) is SGS turbulent thermal diffusivity and is calculated by SGS Prandtl number, $Pr_{SGS} = \upsilon_{SGS}/\alpha_{SGS}$, assumed 0.7 [48]. <…> refers to the time-averaging operation and fluctuation part of the parameters is shown by $(\ldots)'$. For detailed information, the reader is referred to [31]. In the present paper, the buoyancy effect is not considered. The relative effect of buoyancy on the mixed convection (forced and natural) can be explained by the non-dimensional parameter, Richardson (Ri) number. The Ri number ($Ri = Gr/Re^2$) which is the ratio of Grashof number (Gr) to square of Re number was calculated and it is Ri << 1. The Ri << 1 means that the flow is dominated by the force convection and the effect of natural convection can be neglected. Thus, the buoyancy effect on the results is negligible.

The finite volume method is utilized to discretize the governing filtered equations within the open-source CFD package, OpenFOAM V9 [49]. The governing equations are solved by coupling the velocity and pressure via the PIMPLE algorithm [49]. The PIMPLE algorithm within OpenFOAM software is a variation of the PISO algorithm, in which some outer-correction loops are added to maintain the stability of the solver and to prevent divergence. If the number of outer-correction loops is set to zero, the PIMPLE algorithm is equivalent to PISO. In this study, the outer-correction loops are set to 2. The time integration is performed by the second-order backward difference scheme. Spatial discretization is carried out by second-order central differencing. More details about the numerical settings are presented in **Table 1**. The Courant–Friedrichs–Lewy (CFL) number is kept below unity, yielding a non-dimensional physical time step of $\Delta t/(D/U) = 8.3\times10^{-4}$ Upon reaching a semi-steady state condition, time averaging is initiated after transient conditions have passed. In order to omit numerical errors from mean values, all the present numerical simulations are continued at least for 490 non-dimensional time units ($t^* = t \times U/D = 490$) after time-averaging is initiated, where U is the flow mean velocity at the channel inlet.

Table 1 Details of the numerical settings in PIMPLE solver

Numerical settings	**Schemes/Methodology**	**Description/comments**
Pressure-velocity coupling algorithm	PIMPLE algorithm	(Combination of SIMPLE and PISO algorithm)
Time discretization	Backward scheme	Second-order implicit
Convection term discretization	Central differencing scheme	Unbounded second-order
Divergence term discretization	Bounded central difference scheme	Second-order bounded
Laplacian term discretization	Corrected	Unbounded second-order
Time step size, Δt	$\Delta t/(D/U) = 8.3\times10^{-4}$	Satisfies the CFL number condition (CFL < 1)
Sampling time	$t^* = t \times U/D = 490$	70 flow-through times over the porous block

In order to check the effects of the SGS model in the laminar regime, the profiles of υ_{SGS}/υ is shown above the porous-fluid interface at $Y/D = 3.75$ in **Figure 2**(a). As can be seen, the effects of the SGS model vanish completely in the laminar region ($\upsilon_{SGS}/\upsilon = 0$), where there are no turbulence fluctuations (u_{RMS}, v_{RMS}, and Θ_{RMS}). Moreover, the distribution of υ_{SGS}/υ in the transition region, which is less than unity, shows that the grid resolution is fine enough in this region [50, 51].

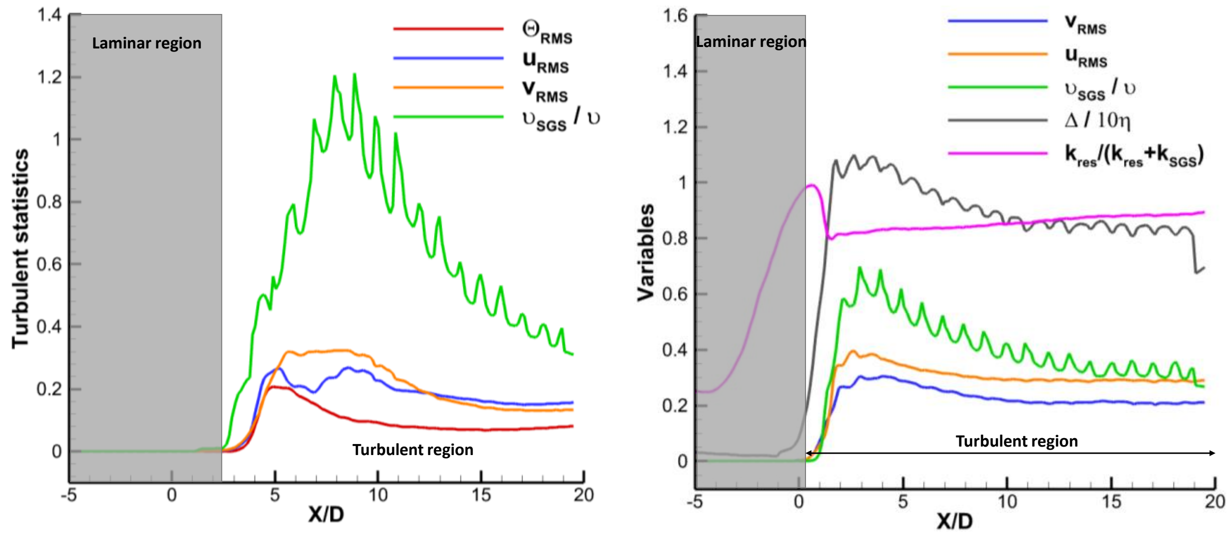

(a) Turbulence statistics at $Y/D = 3.75$

(b) Profiles of u_{rms}, v_{rms}, and different grid resolution criteria at $Y/D = 3.75$

Figure 2 (a) Representation of laminar to turbulence transition above the porous-fluid interface using turbulence statistics at $Re = 3600$; **(b)** Grid resolution assessment with various techniques including $k_{res}/(k_{res} + k_{SGS})$, υ_{SGS}/υ, and ratio of the grid size to the Kolmogorov length scale at $Re = 14400$.

The computational domain for the low- and high-porosity cases at $Re = 3600$ consists of 12.9 and 15.6 million non-uniform grid cells, respectively. Grid resolution of each computational grid is evaluated using different methods, including two-point correlations [50, 52], the ratio of the resolved kinetic energy (k_{res}) to total turbulent kinetic energy (TKE) [53], and the ratio of the SGS eddy viscosity to molecular viscosity [51, 54]. As an example, **Figure 2**(b) displays the ratio of k_{res} to the total turbulence energy ($k_{res} + k_{SGS}$), the ratio of the filter size (Δ) to the Kolmogorov length scale (η), and υ_{SGS}/υ above the porous-fluid interface for the highest Reynolds number. Distribution of $k_{res}/k_{res} + k_{SGS}$ indicates that more than 80% of total turbulent kinetic energy is resolved by the current grid resolution and the filter size is nearly eight times larger than the Kolmogorov length scale. Moreover, the distribution of υ_{SGS}/υ (which is less than 1.2) indicates that the current grid resolution is fine enough. The ratio of the integral length scale (λ), extracted by two-point correlations, to the mean grid size ($\widetilde{\Delta Y}$) is calculated for all six cases (not shown here). The integral length scale represents the resolved energy-containing scales in the motion. The results showed that $\lambda/\widetilde{\Delta Y} \geq 6$, which means that there are at least 6 cells in the resolved scales, ensuring sufficient grid resolution for each case [52]. For 12.9 million grid cells and using 128 CPU cores (Intel Xeon E5-2650 v2 @ 2.60GHz) the simulation time was about 60 days.

2.3 Validation

The experimental testbed of Leu et al. [35] was used to validate the velocity and turbulent statistics obtained from the present pore-scale LES solver. **Figure 3**(a, b) shows that first- and second-order statistics of the velocity of LES calculations are in good agreement with the measured data of Leu et al. [35]. The errors between the LES results and measured data for streamwise and vertical velocities and also turbulent statistics are quantified at two locations $X/D = 1.6$ and 3. The average and maximum errors for the obtained data at $X/D = 16$ are 16.3% and 27.2%, respectively. Also, the corresponding errors for the predicted results at $X/D = 3.0$ are 17.3% and 25.4%. Furthermore, the overall mean Nusselt numbers for the case with blockage ratio $BR = 1.0$ and different Reynolds numbers obtained from the present LES solver are compared against empirical correlations in the literature. [55-62]. As shown in **Figure 3**(c, d) the distribution of the pressure drop and Nu number versus Re number for the current LES solver is in reasonable agreement with the previous studies in the literature.

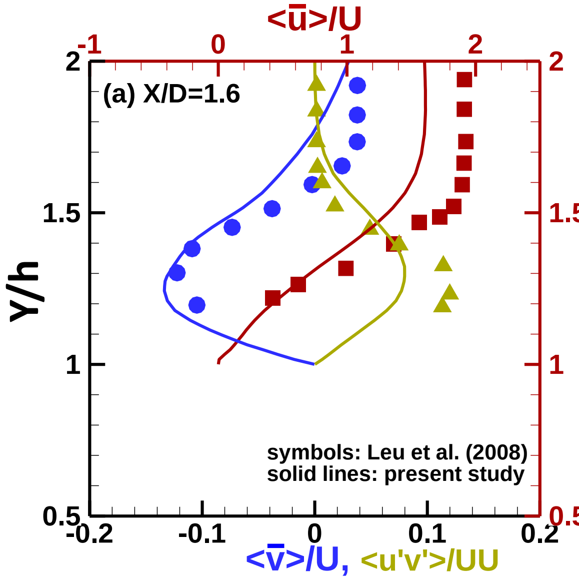

(a) First- and second-order statistics of velocity validation at $X/D = 1.6$

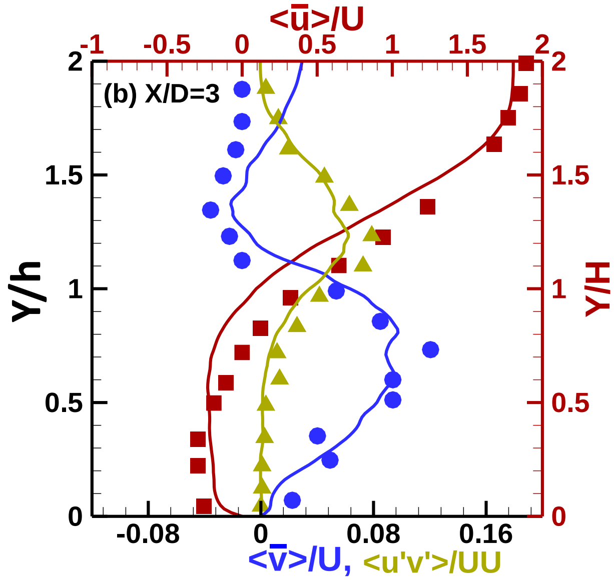

(b) First- and second-order statistics of velocity validation at $X/D = 3.0$

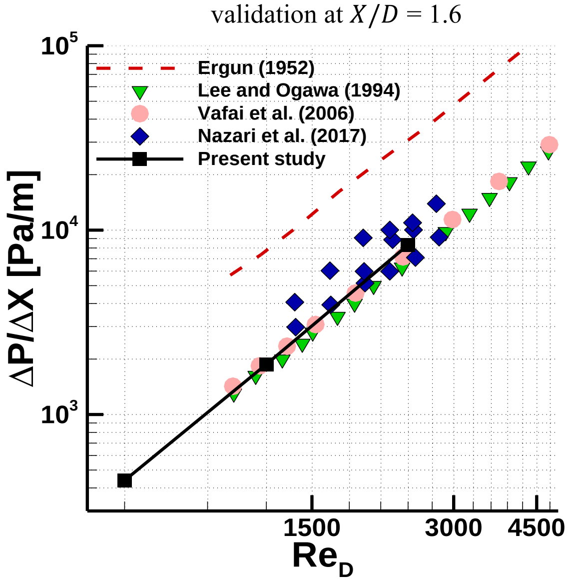

(c) Pressure drop comparison

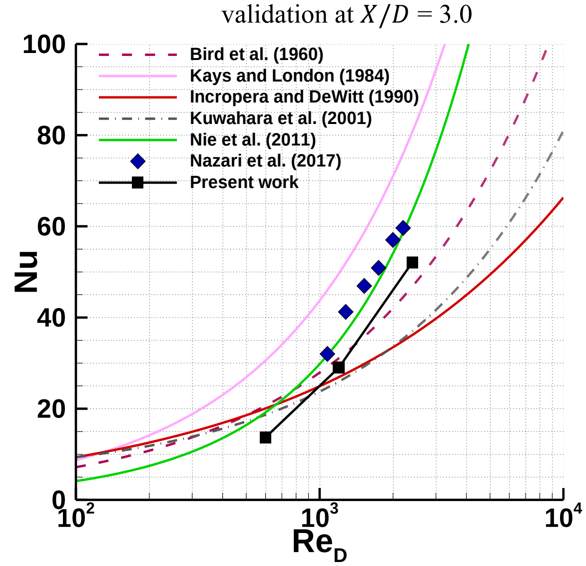

(d) Nu number comparison

Figure 3 (a, b) Comparison of first- and second-order velocity statistics of pore-scale LES study with the measurements of Leu et al. [35]; **(c)** Comparison of Pressure drop in the composite porous-fluid system with available references: Eurgan (1952) [55], Lee and Ogawa (1994) [63], Vafai et al. (2006) [56], Nazari et al. (2017) [62]; **(d)** Comparison of Nu number with available references: Bird et al. [57], Kays and London [58], Incropera and DeWitt [59], Kuwahara et al. [60], Nie et al. [61], Nazari et al. [62].

3 Discussion of results

This section explores the flow and thermal fields in the composite porous-fluid system with a finite porous block. The first sub-section studies the physics of fluid flow including the evolution of coherent structures, flow separation at the leading edge, flow channelling and leakage, and momentum exchange at the porous-fluid interface. The second sub-section examines how these phenomena affect the system's thermal characteristics. This sub-section includes the distribution of local and overall Nusselt (Nu) numbers, turbulent heat flux, and first- and second-order temperature statistics.

3.1 Flow field

Figure 4 shows the hairpin coherent structures identified by instantaneous iso-surface of $Q = 0.5 \times (\|\Omega\|^2 - \|S\|^2)$ criterion and colored by non-dimensional instantaneous temperature ($\bar{\Theta}$). It also depicts the non-dimensional time-averaged streamwise velocity contours ($<\bar{u}>/U$) for different Re numbers and two porosities. For all cases, the forest of hairpin coherent structures is observed over the interface. The hairpin structure consists of three components: head, necks, and legs; The hairpin head lies at the furthest distance from the interface; The hairpin necks connect the hairpin legs and head; The third part is the hairpin legs which is the closest part to the porous-fluid interface.

The effect of Re number and porosity on the flow features over the porous-fluid interface is remarkable. For the low-porosity case at Re = 3600, two distinct regions can be recognized. In region#1 ($0 < X/D < 10.4$), the shear layer rolls up after the flow separation at the leading edge to generate hairpin structures with the dominant spanwise vorticity at their heads. In this region, the heads of hairpins are oriented toward the leading edge (**Figure 4**(a)), where $\beta \cong 122^o$ (i.e., β is the angle of the connecting line between the hairpin's leg and head with regard to the horizontal direction). In contrast, in region#2 ($10 < X/D < 20$), the orientation of the hairpin heads is completely different (see **Figure 4**(a)), pointing toward the trailing edge of the porous block, where $\beta \cong 34^o$.

In **Figure 4**(a, c, e), the velocity contours on the trough planes also illustrate regions#1 and #2 over the porous-fluid interface. Region#1 with organised hairpin structures is characterised by the flow separation at the leading edge of the porous block and the formation of a turbulent separation bubble (TSB) over the interface. Whilst, in region#2 with unorganised hairpin structures, the boundary layer attaches to the interface and starts redeveloping. In the previous study by the authors [31], owing to the small porous length (LR = 10) and low Re number (Re = 3600), the separated flow does not attach to the interface, resulting in lack of boundary layer redevelopment. The findings in [31] are consistent with the flow features in region#1. However, the higher porous length (LR = 20) in the present study allows the turbulent boundary layer to redevelop over the interface after reattaching at $X/D \sim 10.4$. Furthermore, **Figure 4**(a, c, e) indicates that by increasing the Re number, the length of the region#1 is shortened; for instance, at Re = 14400, it is extended merely up to $X/D \cong 5.8$.

Figure 4(b, d, f) demonstrates a forest of unorganised hairpin coherent structures for high-porosity cases. The pattern of hairpin structures corresponds to the arrangement of counter-rotating vortex pairs (CRVPs) above the interface [30, 31]. Moreover, flow leakage quantification for high- and low-porosity cases (discussed in **Figure 6**) indicates that the flow leakage reduces drastically for high-porosity cases, which disorders the organised pattern of CRVPs. Hence, disordered hairpins for high-porosity cases are associated with lower flow leakage and unorganised CRVPs. Furthermore, for high-porosity cases, the orientation of the hairpin heads is different. Near the leading edge due to the flow acceleration, the heads of the hairpins point toward the trailing edge of the porous block ($\beta < 90^o$), while far from the leading edge, it is nearly vertical with $\beta \cong 90^o$. It should be noted that distinct regions#1 and #2 are not identified at any Re number for high-porosity cases.

Finally, **Figure 4** shows that increasing the porosity not only affects the coherent structures on the porous-fluid interface but also influences the channelling effect trends inside the porous block. For low-porosity cases (**Figure 4**(a, c, e)), the channelling effect dominates the flow pattern inside the porous block on the trough plane; thus, producing streamwise-oriented high-momentum paths in the horizontal direction [31]. Whereas, for the high-porosity cases distinct channelling flows are not identified inside the porous region as clearly as those observed in the low-porosity cases (**Figure 4**(b, d, f)).

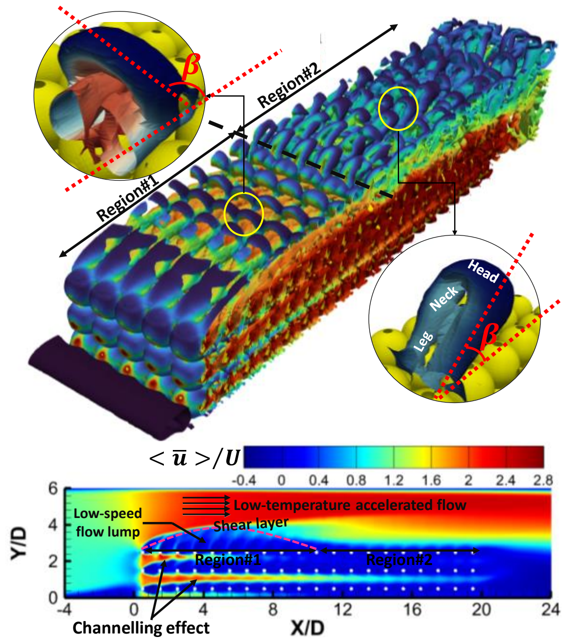

(a) Re = 3600, Low porosity

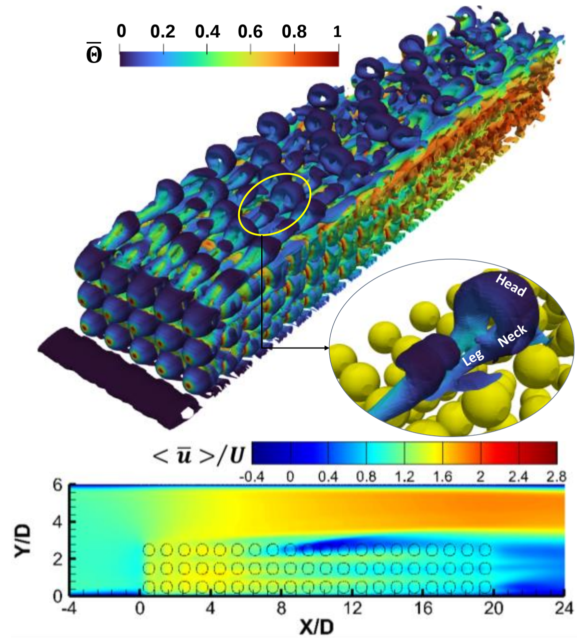

(b) Re = 3600, High porosity

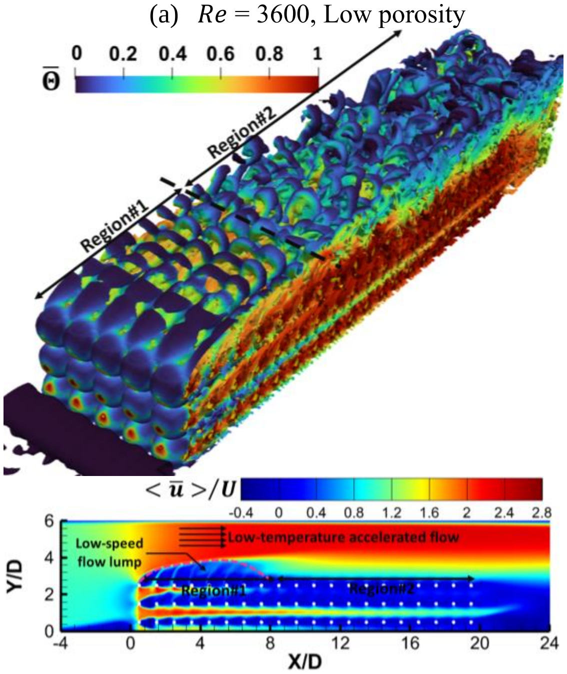

(c) Re = 7200, Low porosity

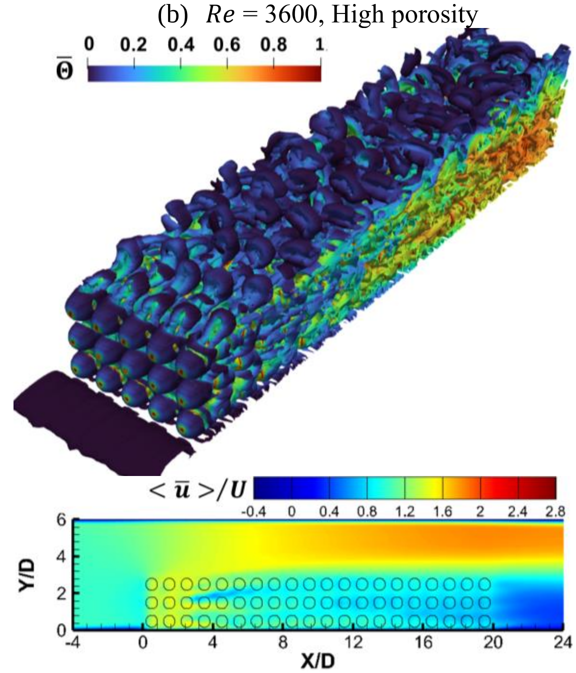

(d) Re = 7200, High porosity

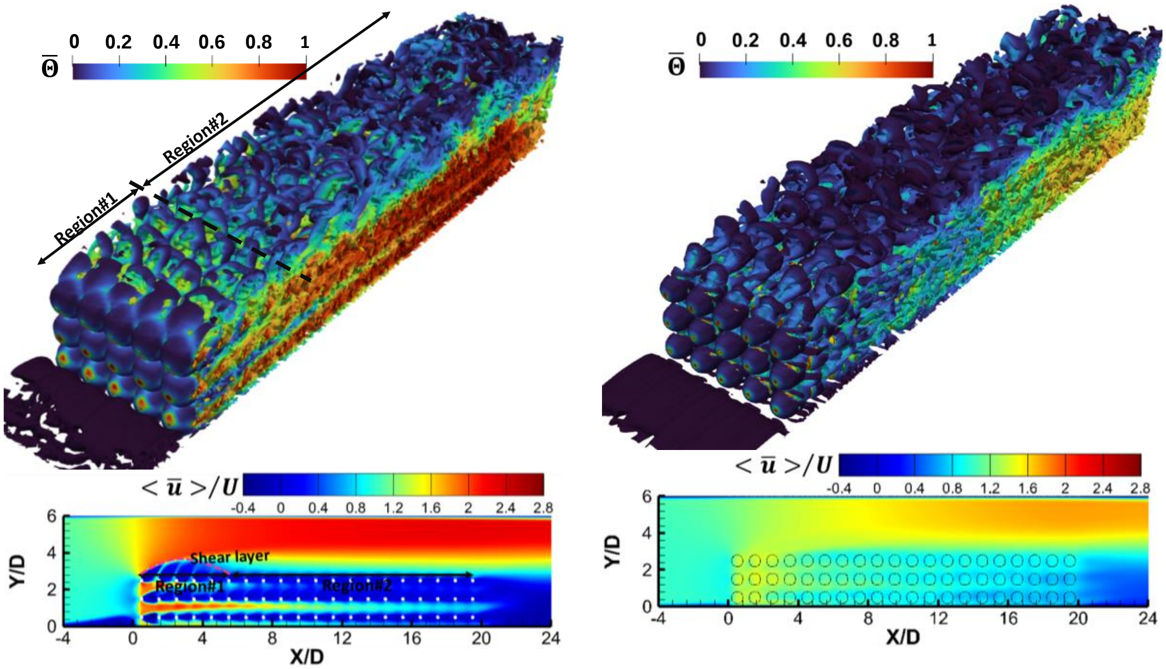

(e) Re = 14400, Low porosity (f) Re = 14400, High porosity

Figure 4 Three-dimensional hairpin coherent structures identified by instantaneous iso-surface of $Q = 0.5 \times (\|\Omega\|^2 - \|S\|^2)$ criterion coloured by instantaneous non-dimensional temperature ($\bar{\Theta}$) for three Re numbers and two porosities; below each figure the contour of non-dimensional time-averaged streamwise velocity ($< \bar{u} >/U$) shows the channelling effect and flow leakage for each case; **(a, c, e)** Low porosity; **(b, d, f)** High porosity.

Figure 5 depicts the evolution of hairpin structures through the turbulent boundary layer development over the porous-fluid interface for the low-porosity case at Re = 3600. In addition, the auto-correlation (R_{vv}) of vertical velocity fluctuations (v') around the hairpin head (Y/D = 4.0) is displayed at three different streamwise locations, $X/D = 5$, 9 and 14. The R_{vv} is defined as follows:

$$R_{vv}(\tau) = \frac{< v'(t).v'(t+\tau) >}{\sqrt{< v'(t)^2 >< v'(t+\tau)^2 >}} \tag{5}$$

It is seen in **Figure 5** that the orientations of hairpin heads are different in regions#1 and #2. In region#1 the streamwise velocity profiles (not shown here) exhibit an inflexion point close to the hairpin head. This inflection point demonstrates that the mean convective velocity near the hairpin legs and necks is higher than that around the head. Therefore, in region#1 the heads of hairpins are oriented toward the leading edge with $\beta \cong 122^o$. In contrast, in region#2 the mean convective velocity around the hairpin head increases monotonically and surpasses the velocity of legs and necks, resulting in the hairpin head pointing to the trailing edge with $\beta \cong 34^o$. Moreover, the comparison of R_{vv} at X/D = 5 (in region#1) with X/D = 14 (in region#2) indicates that hairpin structures in region#1 convect faster than those in region#2. Also, according to time scales in **Figure 5** and mean convective velocities (not shown here), the distance between two successive hairpin heads in region#2 is greater than that in region#1. For example, in region#1 at X/D = 5 the distance is 1.21D, whereas it is 1.54D in region#2 at X/D = 14.

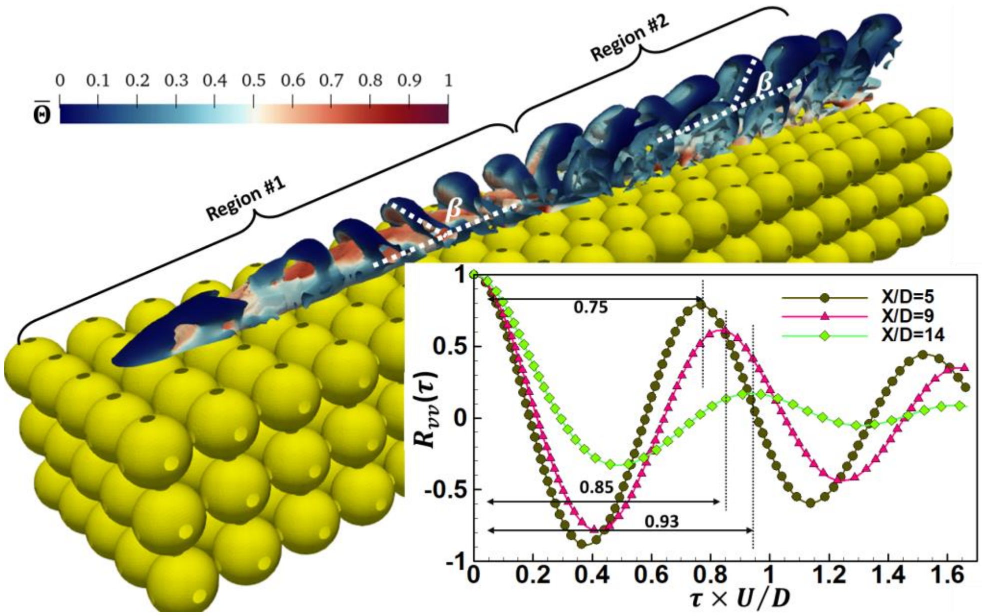

Figure 5 Evolution of hairpin structures on the porous-fluid interface, and auto-correlation plots around the hairpin head (Y/D = 4) at different streamwise locations for the low-porosity case at Re = 3600.

To investigate the interactions between porous and non-porous regions, the first-order statistics of the velocity field are calculated. **Figure 6** displays the profile of non-dimensional time-averaged vertical velocity ($<\bar{v}>/U$) on the porous-fluid interface. **Figure 6**(a, c, e) and **Figure 6**(b, d, f) are associated with the low- and high-porosity cases, respectively. The tables in **Figure 6** indicate the relative flow rates that leak from the porous region into the non-porous region up to different streamwise locations. In **Figure 6**, $Q_{in} = \int_0^{3D} \int_{-2.5D}^{2.5D} <\bar{u}(Y,Z)> dZdY$ and $Q_{lX} = \int_0^{X} \int_{-2.5D}^{2.5D} <\bar{v}(X,Z)> dZdX$ are defined as time-averaged flow rates, entering the porous media from the frontal face, and leaking from the X-percentage of the porous-fluid interface, respectively [31]. **Figure 6**(a, c, e) notifies that for low-porosity cases, region#1 and region#2 are characterised by higher and lower vertical velocities, respectively. Further, increasing the Re number from 3600 to 14400, shortens the length of region#1 from $X/D \sim$ 10.4 to 5.6, as was seen in **Figure 4**. As evident in **Figure 6**(b, d, f), high-porosity cases display much lower vertical velocities, especially in the first half of the porous length, compared to the low-porosity cases. No notable differences are detected among high-porosity cases of different Re numbers on the first half of the porous length. However, it should be emphasized that in the second half of the porous length at Re = 7200 and 14400 some portion of the flow from the non-porous region penetrates the porous region (in contrast to the flow leakage), which is marked by "A" in **Figure 6**(d, f). In low-porosity cases, the flow penetration from non-porous regions into porous regions occurs for a shorter portion of porous length near the trailing edge compared to high-porosity cases (marked region "B" in **Figure 6**(c, e)).

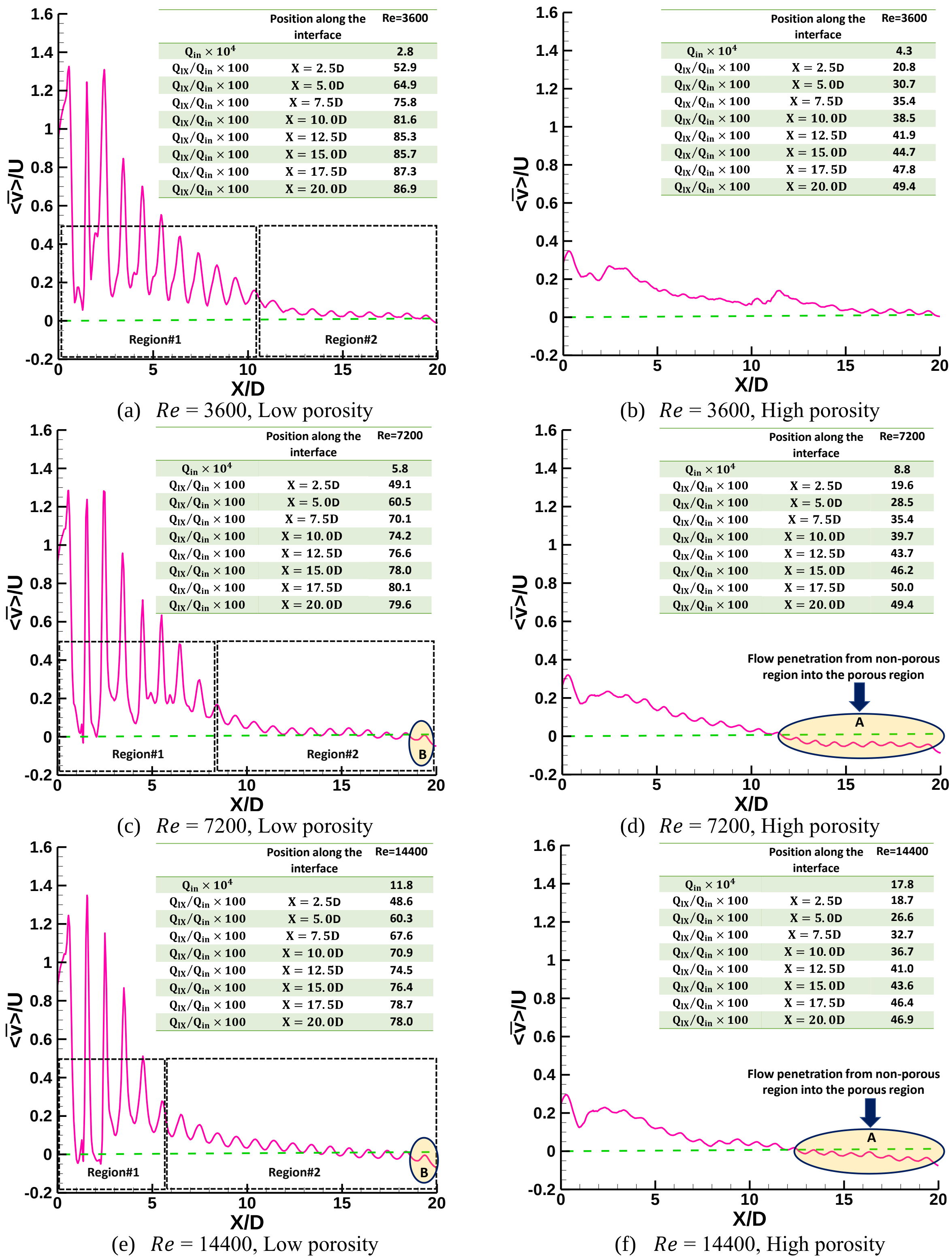

(a) Re = 3600, Low porosity (b) Re = 3600, High porosity
(c) Re = 7200, Low porosity (d) Re = 7200, High porosity
(e) Re = 14400, Low porosity (f) Re = 14400, High porosity

Figure 6 Non-dimensional time-averaged vertical velocity ($< \bar{v} >/U$) profiles along the porous-fluid interface for three Re numbers and two porosities; **(a, c, e)** Low porosity; **(b, d, f)** High porosity.

Figure 7 represents the relative flow rate (Q_{lX}/Q_{in}) that leaks from the porous region into the non-porous region across the porous-fluid interface at different streamwise locations. Low-porosity cases possess significantly higher flow leakage, nearly twice as much as high-porosity cases. For low-porosity cases, around 82% of the flow entering the porous block leaks from the porous-fluid interface before it reaches the end of the porous region, but for high porosities, the leakage drops to 49%. Moreover, the flow leakage of low-porosity cases ranges between 48% and 87% from the leading edge to the trailing edge, while that of high-porosity cases varies between nearly 19% and 49%. The effect of the Re number on the flow leakage is more pronounced for low-porosity cases than those for high-porosity cases, except near the leading edge. For instance, as the Re number increases from 3600 to 14400, the flow leakage for low-porosity cases reduces by about 10%, whilst, for high-porosity cases, it decreases by about 5%.

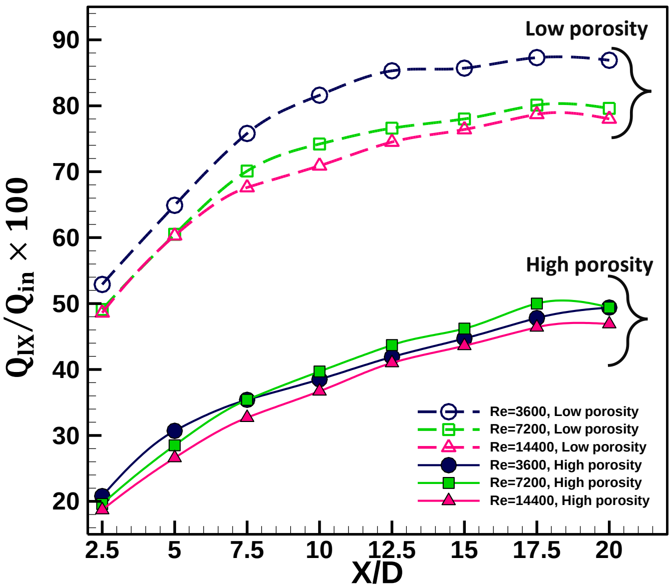

Figure 7 Flow leakage ratio (Q_{lx}/Q_{in}) for low- and high-porosity cases at three Re numbers.

To further investigate the interaction between porous and non-porous regions, the following two figures focus on the second statistics of the velocity field. For this purpose, the temporal cross-correlation of vertical velocity fluctuations is calculated for different probe pairs in regions#1 and #2. Temporal cross-correlation (also called space-time correlation) is a statistical technique for quantifying and exploring the coupling of spatial and temporal scales of motion in turbulence. Temporal cross-correlation is often employed to explore the dynamics of information transfer by turbulent structures. For two arbitrary points A and B, the temporal cross-correlation of vertical velocity fluctuations, $R_{A,B}(\tau)$, is defined as follows:

$$R_{A,B}(\tau) = \frac{< v_A{}'(t).v_B{}'(t+\tau) >}{\sqrt{< v_A{}'(t)^2 >< v_B{}'(t+\tau)^2 >}} \tag{6}$$

Two probes (P3 and P4) were placed beneath the interface and one probe above the interface(P3) for calculation of the temporal cross-correlations. **Figure 8**(a, b) exhibits the location of probes (P1-P4) in regions#1 and #2 superimposed on the instantaneous streamwise velocity contours for low-porosity cases at Re = 3600 and 14400, respectively. For instance, $R_{P1,P3}$ illustrates the temporal cross-correlation between probe P1 (over the interface) and P3 (beneath the interface). In **Figure 8**(c, d), the $R_{P1,P3}$ and $R_{P3,P4}$ are presented for both Re = 3600 and 14400. The non-zero values of $R_{P1,P3}$ in **Figure 8**(c, d) highlight that there is a strong correlation between porous (P3) and non-porous (P1) regions, representing the exchange of flow properties (momentum and energy) through the porous-fluid interface. Additionally, trends of temporal cross-correlation show that the dynamics of information transfer (momentum and energy transfer) in regions#1 and #2 are influenced by the flow leakage and Re numbers.

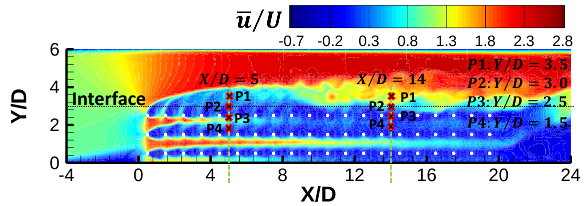

(a) Re = 3600, location of probes (P1-P4)

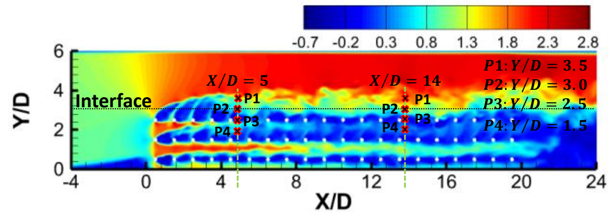

(b) Re = 14400, location of probes (P1-P4)

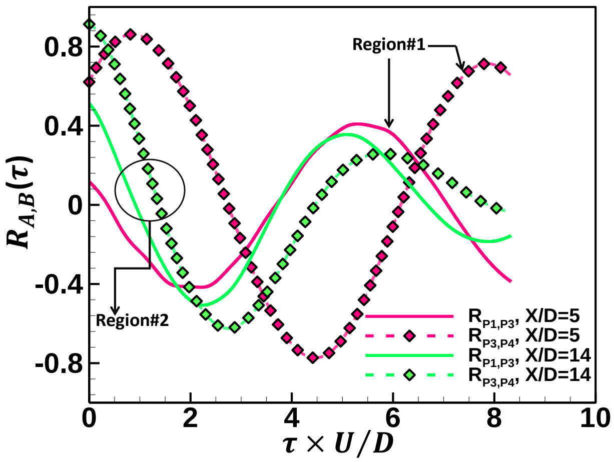

(c) Re = 3600, region#1 (X/D = 5) and region#2 (X/D = 14)

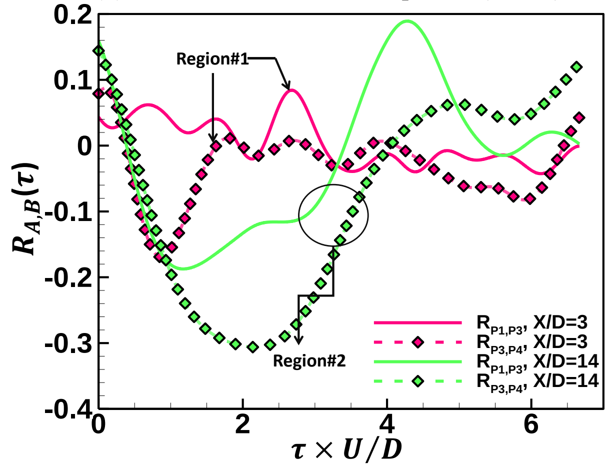

(d) Re = 14400, region#1 (X/D = 3) and region#2 (X/D = 14)

Figure 8 (a, b) Instantaneous velocity contours and location of selected probes (P1-P4) for temporal cross-correlation calculations at Re = 3600 and Re = 14400, respectively; **(c)** Temporal cross-correlations of (P1, P3) and (P3, P4) for Re = 3600 at X/D = 5 and 14; **(d)** Temporal cross-correlations of (P1, P3) and (P3, P4) for Re = 14400 at X/D = 3 and 14; Probes P3 and P4 are beneath the interface at Y/D = 2.5 and Y/D = 2 respectively whereas probe P3 is above the interface at Y/D = 3.5.

To further investigate the physics behind the momentum exchange across the porous-fluid interface and quantify the correlations between the porous and non-porous regions, the quadrant analysis [64] and Pearson linear correlation coefficient [65] are employed. **Figure 9** shows the contours of the turbulent joint probability density function (JPDF) of non-dimensional velocity fluctuations, $\sigma_u = u'/u_{RMS}$ and $\sigma_v = v'/v_{RMS}$. The JPDFs are presented in regions#1 and #2 at different elevations namely: $0.5D$ below the interface (Y/D = 2.5); on the interface (Y/D = 3.0); and $1.0D$ over the interface in the shear layer (Y/D = 4.0). In the quadrant analysis, the velocity fluctuations u' and v' are divided into four quadrants based on the signs of their instantaneous values. The first quadrant Q1 corresponds to $u' > 0$, $v' > 0$, called outward intersection event. The second quadrant Q2 is associated to $u' < 0$, $v' > 0$, called ejection event. The third quadrant Q3 corresponds to $u' < 0$, $v' < 0$, called inward intersection event, and the fourth quadrant Q4 with $u' > 0$, $v' < 0$ is known as sweep event. The ejection events transport a low-momentum fluid upwards, while the sweep events transport a high-momentum fluid downwards. The outward intersection events transport a high-momentum fluid upwards. Moreover, for signals Λ and Γ having means $\bar{\Lambda} = \sum_{i=1}^{n} \Lambda_i/n$ and $\bar{\Gamma} = \sum_{i=1}^{n} \Gamma_i/n$, the Pearson linear correlation coefficient, ϒ, is defined as:

$$\Upsilon = \frac{\sum_{i=1}^{n}(\Lambda_i - \bar{\Lambda})(\Gamma_i - \bar{\Gamma})}{\left\{\sum_{i=1}^{n}(\Lambda_i - \bar{\Lambda})^2 \sum_{i=1}^{n}(\Gamma_i - \bar{\Gamma})^2\right\}^{1/2}} \tag{7}$$

Figure 9(a, b) shows the JPDFs of streamwise and vertical velocity fluctuations far from the interface for the low-porosity case at Re = 3600. The elliptical JPDFs and high negative correlation coefficients (ϒ) indicate that the fluctuations are anti-correlated, and the momentum is exchanged by sweep/ejection events in both regions#1 and #2. By the ejection event, the low-speed fluid ($-u'$) over the interface moves upward ($+v'$). Whereas, by sweep event, the high-speed fluid ($+u'$) above the shear layers moves downward ($-v'$).

This observation shows the bottom-up and top-down turbulence interactions associated with the hairpin head that will be discussed in **Figure 15**(b).

On the interface at Y/D = 3.0, two different momentum exchange mechanisms can be recognized in regions #1 and #2 in **Figure 9**(c, d). In region#1, the JPDF contour in **Figure 9**(c) has a semi-elliptical shape, along the line $\sigma_u = \sigma_v$ with Υ = 0.19. This trend confirms the induced outward/inward intersection events which indicate the time-depended flow leakage. However, in region#2, the elliptical contour of JPDF in **Figure 9**(d) is along the line $\sigma_u = -\sigma_v$ with Υ = -0.66. This means that the velocity fluctuations are anti-correlated, and the momentum exchange is governed by sweep/ejection events. The different orientation of JPDFs in **Figure 9**(c, d) highlights the effects of TSB and flow leakage in region#1, and the reattachment (and redevelopment) of the boundary layer in region#2, as also discussed in **Figure 4**.

Below the interface in regions#1 and #2, the contours of JPDF in **Figure 9**(e, f) illustrate elliptical contours along $\sigma_u = \sigma_v$ with positive Υ. This means that beneath the interface, outward/inward intersection events are dominant in both regions#1 and #2. However, due to the positive mean flow leakage, there is a strong tendency for upward motion ($+v'$) of the high-momentum streamwise-oriented flow ($+u'$) from porous region into the non-porous region. Furthermore, in region#1 due to the stronger flow leakage, Υ is higher than that in region#2, which is consistent with previous findings in **Figure 6**.

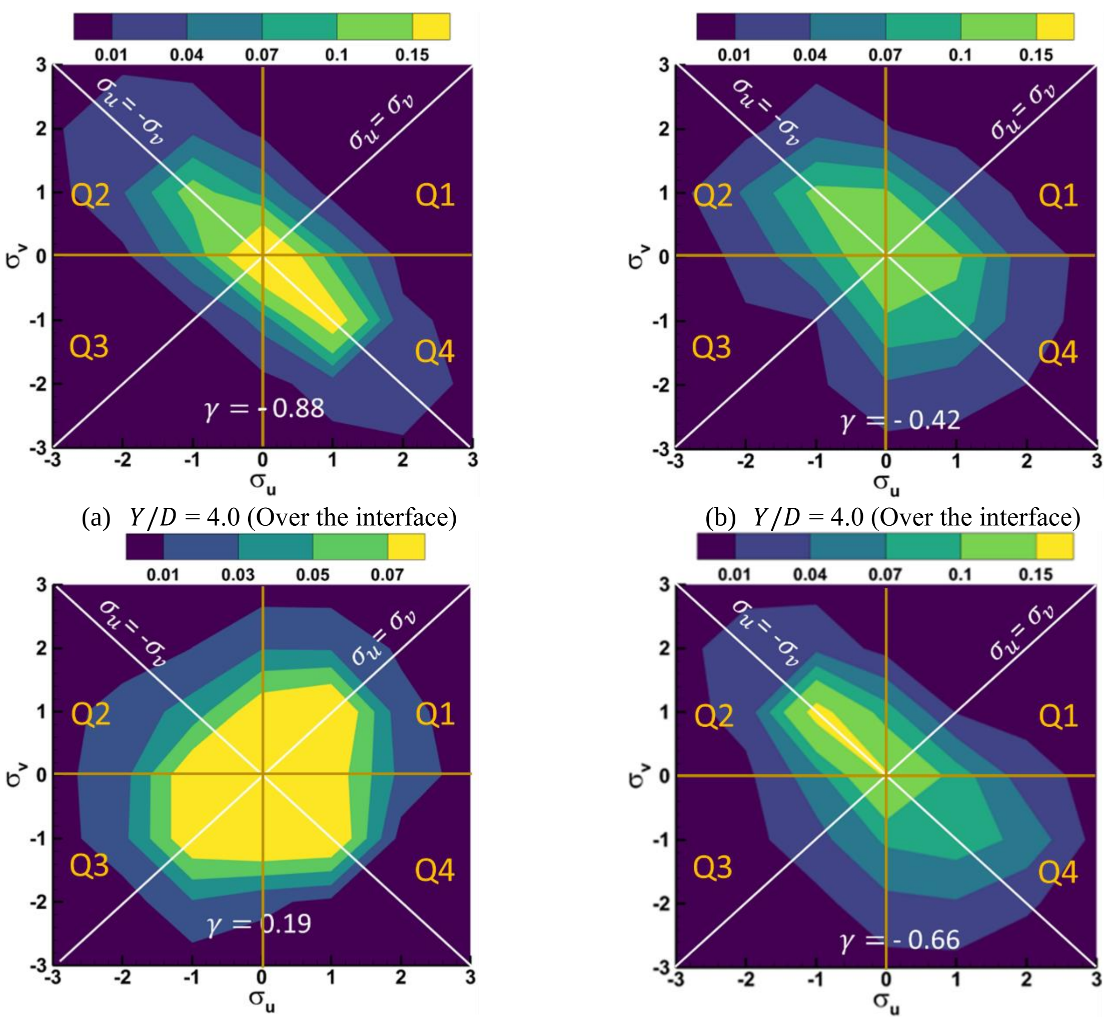

(a) Y/D = 4.0 (Over the interface)

(b) Y/D = 4.0 (Over the interface)

(c) Y/D = 3.0 (On the interface)

(d) Y/D = 3.0 (On the interface)

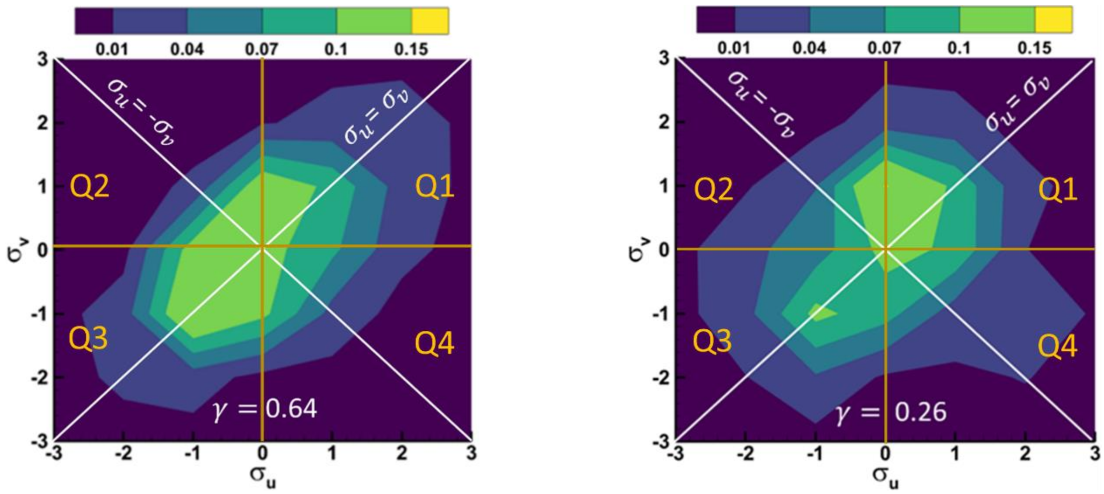

(e) Y/D = 2.5 (Beneath the interface) (f) Y/D = 2.5 (Beneath the interface)

Figure 9 Contours of JPDF of $\sigma_u = u'/u_{RMS}$ and $\sigma_v = v'/u_{RMS}$ in regions#1 and #2 on the trough plane at different elevations for the low-porosity case at Re = 3600; **Left**: Region#1 at X/D = 5; **Right**: Region#2 at X/D = 14 .

Regarding the origin of the outward/inward interactions in **Figure 9**(e, f), details of flow behaviour beneath the porous-fluid interface are shown in **Figure 10.** As can be seen, the streamlines of the mean flow motion in regions#1 and #2 demonstrate a positive (i.e., from the porous region to the non-porous region) time-averaged flow leakage (see **Figure 10**(c, d)). However, the authors believe that the flow leakage has an unsteady pulsating nature over time and the flow behaviour beneath the interface is not only governed by the pulsating nature of flow leakage but also by the porous structures, simultaneously. Therefore, the origin of the outward/inward interactions in **Figure 9**(e, f) is related to the local turbulence motions (downwards and upwards flow motions in **Figure 10**(c, d)) generated by the spheres beneath the porous-fluid interface and unsteady flow leakage.

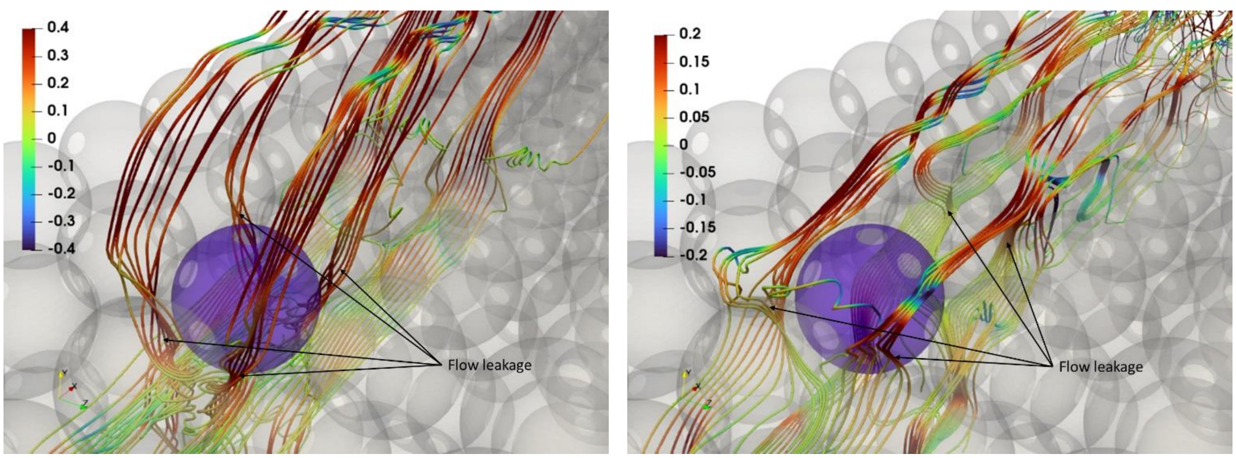

(a) Streamlines around sphere5-1in region#1 (b) Streamlines around sphere14-1in region#2

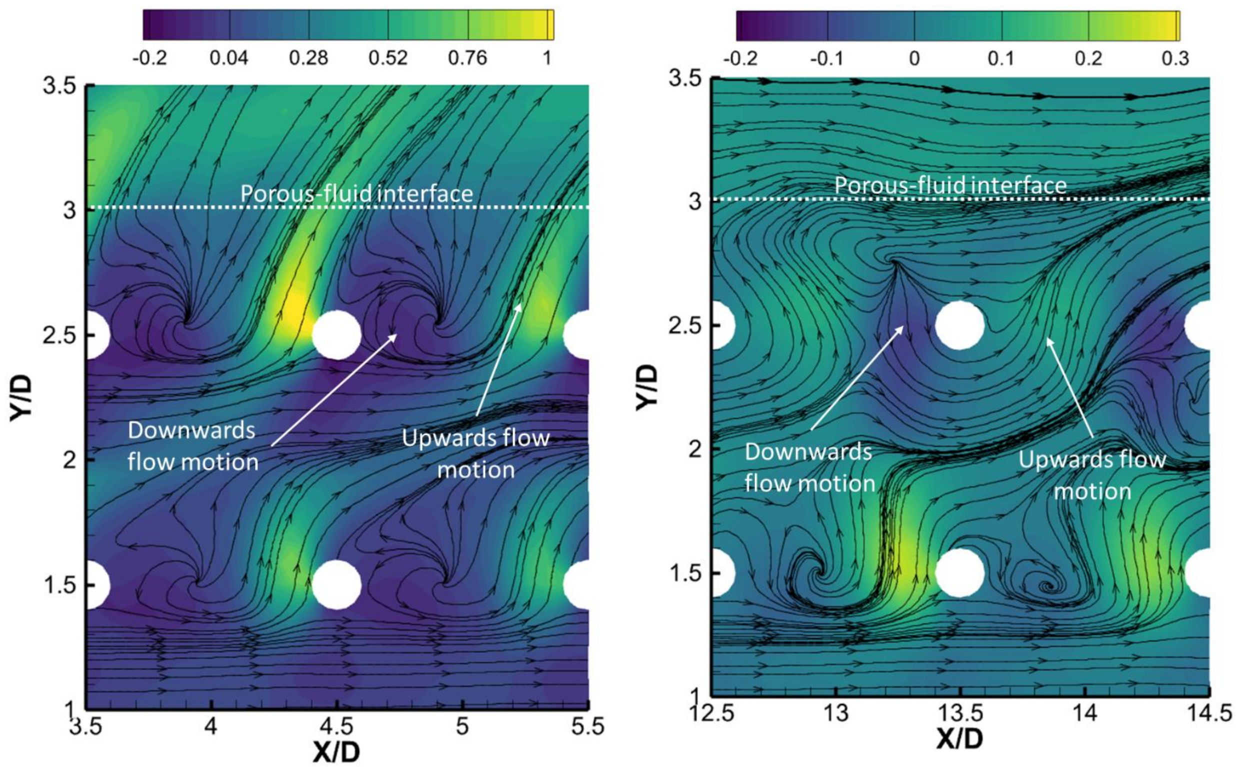

(c) Contour of vertical velocity around sphere5-1 in region#1

(d) Contour of vertical velocity around sphere14-1 in region#2

Figure 10 Flow behaviour around Sphere5-1 and Sphere14-1 beneath the porous-fluid interface regarding JPDF of $\sigma_u = u'/u_{RMS}$ and $\sigma_v = v'/u_{RMS}$ in **Figure 9**(e, f) on the trough plane for the low-porosity case at Re = 3600; **Left**: Region#1; **Right**: Region#2; Sphere "i-j" indicates the sphere's location in the i^th column and j^th row of the porous block (e.g., sphere5-1 means the 5^th column in the porous block and the first row). The first row is located on the porous-fluid interface and the first column is located at the leading edge of the porous block.

3.2 Thermal field

Figure 11 displays the side-view contours of non-dimensional time-averaged streamwise turbulent heat flux and temperature fluctuations at different locations at Re = 3600. **Figure 11**(a-d) and **Figure 11**(e-h) correspond to the low and high porosities, respectively. The streamlines illustrate how the counter-rotating vortex pairs (CRVPs) originate from the porous region and push upwards into the non-porous region. **Figure 11**(a, b) shows that there is an arch-shaped area of high turbulent fluctuations (marked as "Max#1") above the core of the CRVPs in region#1 (X/D = 5.5), which corresponds to the hairpin head. High values of turbulence statistics around the hairpin head at Y/D = 4.0 in **Figure 11**(a, b) originate from the strong shear layer between the low-speed flow lump in the TSB and accelerated flow above the TSB (see **Figure 4**(a) for the location of low-speed flow lump and accelerated flow). In addition, in **Figure 11**(a, b), the well-organised CRVPs' patterns in region#1 exhibit organised hairpin structures, explained in **Figure 4**(a). Whereas, **Figure 11**(c, d) indicates that region#2 (X/D = 15.5) is characterised by unorganised CRVPs, resulting in disordered hairpin structures (see **Figure 4**(a)). Finally, it is seen that in region#1, which is characterised by high flow leakage and organised CRVPs, the turbulent fluctuations peak away from the interface ("Max#1"). Whereas, in region#2 with negligible flow leakage, the location of maximum turbulent fluctuations approaches the porous-fluid interface ("Max#2" in **Figure 11**(c, d)). For high-porosity cases in **Figure 11**(e-h), the unorganised CRVPs correspond to disordered hairpin structures, especially at X/D = 15.5. This observation is consistent with the previous discussions in **Figure 4**(b). Besides, by moving forward along the porous length, the maximum values of turbulence statistics approach the porous-fluid interface, similar to the low-porosity cases.

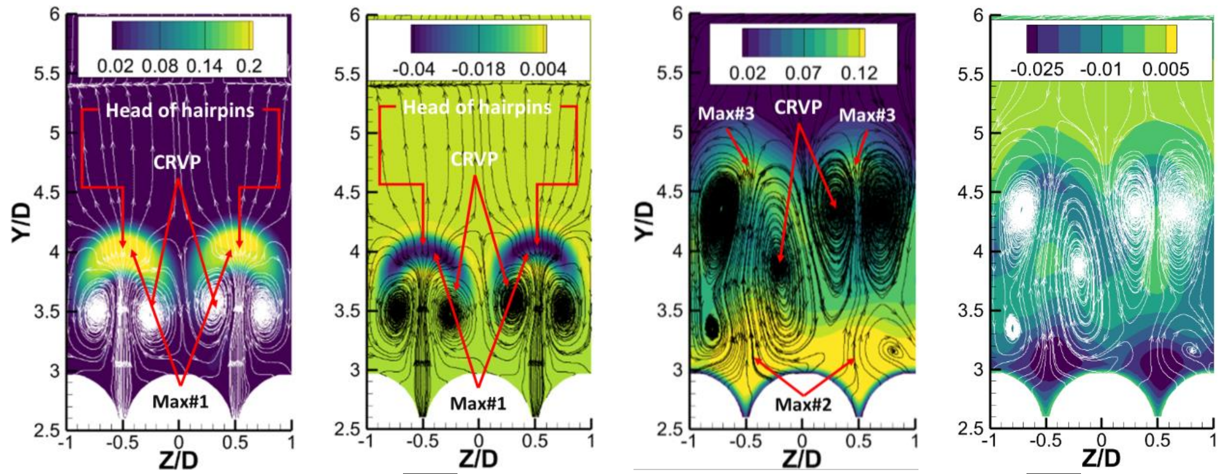

(a) θ_{RMS} at X/D = 5.5 (b) $<\overline{u^{*\prime}\theta^{\prime}}>$ at X/D = 5.5 (c) θ_{RMS} at X/D = 15.5 (d) $<\overline{u^{*\prime}\theta^{\prime}}>$ at X/D = 15.5

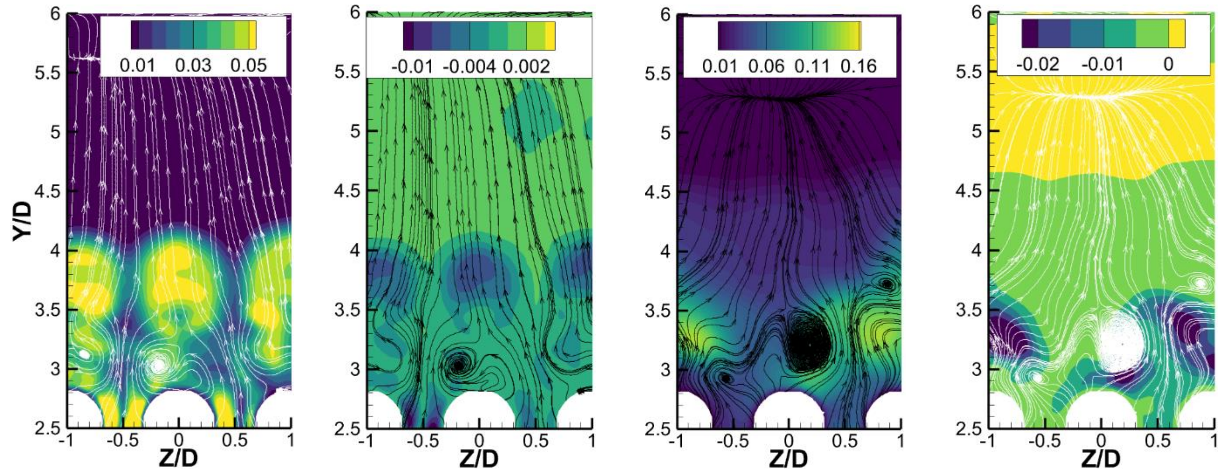

(e) θ_{RMS} at X/D = 5.5 (f) $<\overline{u^{*\prime}\theta^{\prime}}>$ at X/D = 5.5 (g) θ_{RMS} at X/D = 15.5 (h) $<\overline{u^{*\prime}\theta^{\prime}}>$ at X/D = 15.5

Figure 11 CRVP structures shown by streamlines overlaid on temperature fluctuations (θ_{RMS}) and streamwise turbulent heat flux ($<\overline{u^{*\prime}\theta^{\prime}}>$) contours over spanwise planes at two different locations (X/D 5.5 and 15.5) for Re = 3600; **(a-d)** Low porosity; **(e-h)** High porosity.

Figure 12(a, b) displays the contours of instantaneous temperature and root-mean-squared (RMS) of temperature fluctuations on the trough plane for Re = 3600 and Φ = 53%, **Figure 12**(a) illustrates different flow features in regions#1 and #2. In region#1, the instantaneous temperature distribution highlights the flow separation at the leading edge of the porous block and the onset of the Kelvin-Helmholtz instability [31]. In **Figure 12**(b), the maximum temperature fluctuations in region#1 (Max#1) locate away from the porous-fluid interface. The observations for region#1 are consistent with the previous findings for short porous length with LR = 10[30, 31]. In region#2, the location of maximum temperature fluctuations (Max#2) approaches the interface in **Figure 12**(b), where the boundary layer is reattached to the interface. The observations for region#2 are consistent with the findings for fully-developed porous channel flows observed in previous works in the literature [19, 24, 25, 28, 66]. **Figure 12**(a, b) also shows that the gradient of temperature and its fluctuations across the interface is sharper in region#2 compared to that in region#1.

The difference between regions#1 and #2 is also visible in the organised and unorganised iso-surface of instantaneous vertical velocity fluctuations in **Figure 12**(c). **Figure 12**(c) illustrates that there are no turbulence fluctuations for Re = 3600 in region#1 after the flow separation at the leading edge and before the K-H instability's onset [31]. While organised alternating fluctuations are observed with the advent of

K-H instabilities. The observations in region#1 and region#2 for the low-porosity case with Re = 3600 are also valid for higher Re numbers. However, when the Re number increases the length of region#1 is shortened and turbulence production initiates just after the leading edge of the porous block.

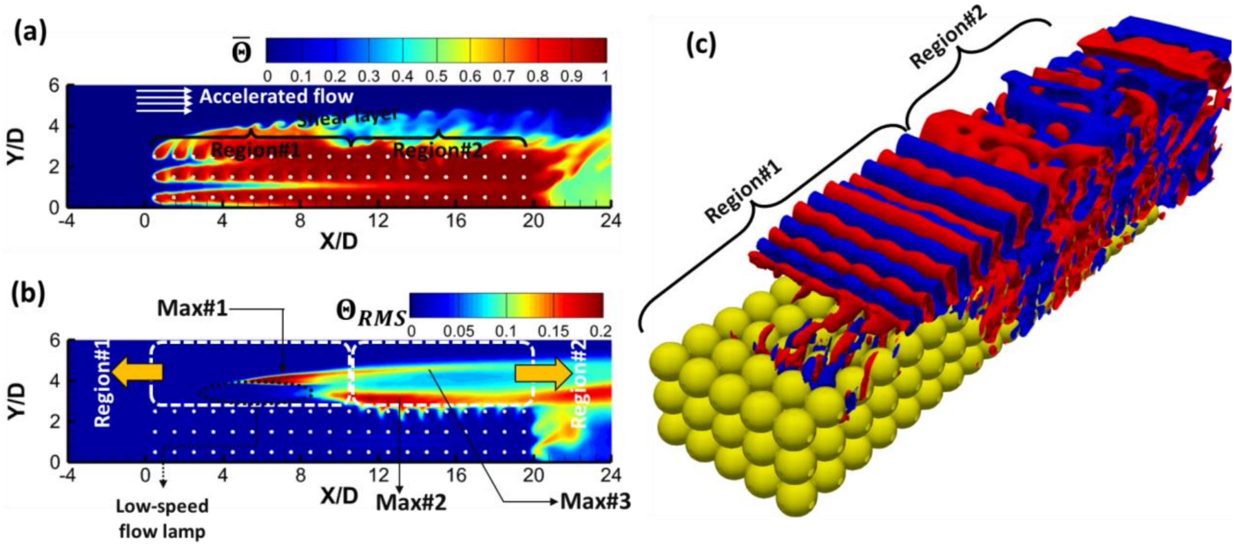

Figure 12 (a, b) Contour of non-dimensional instantaneous temperature ($\bar{\Theta}$) and temperature fluctuations (Θ_{RMS}), respectively, at Re = 3600 and low porosity (Φ = 53%); **(c)** Iso-surface of instantaneous vertical velocity fluctuations; **Blue**: negative value; **Red**: Positive value. The figure represents the effect of flow evolution over the porous-fluid interface on the temperature distribution and its fluctuations.

Figure 13(a, b) displays instantaneous temperature contours and root-mean-squared (RMS) fluctuations on the trough plane for the high-porosity case at Re = 3600. Temperature distributions for the high-porosity case are significantly different from those for the low-porosity case. For the high-porosity case, there is no flow separation at the leading edge of the porous block, and the incoming low-temperature flow can easily enter the porous block from its frontal face. Moreover, maximum temperature fluctuations occur over the interface in the second half of the porous length. Also, some areas with high-temperature fluctuations, marked as "A", are observed inside the porous block in **Figure 13**(b). The irregular iso-surface of instantaneous vertical velocity fluctuations along the porous length in **Figure 13**(c) is consistent with the disordered hairpin structures and CRVPs' patterns, discussed in **Figure 4** and **Figure 11**, respectively. As shown in **Figure 13**(c), distinct regions#1 and #2 are not recognised for high-porosity cases.

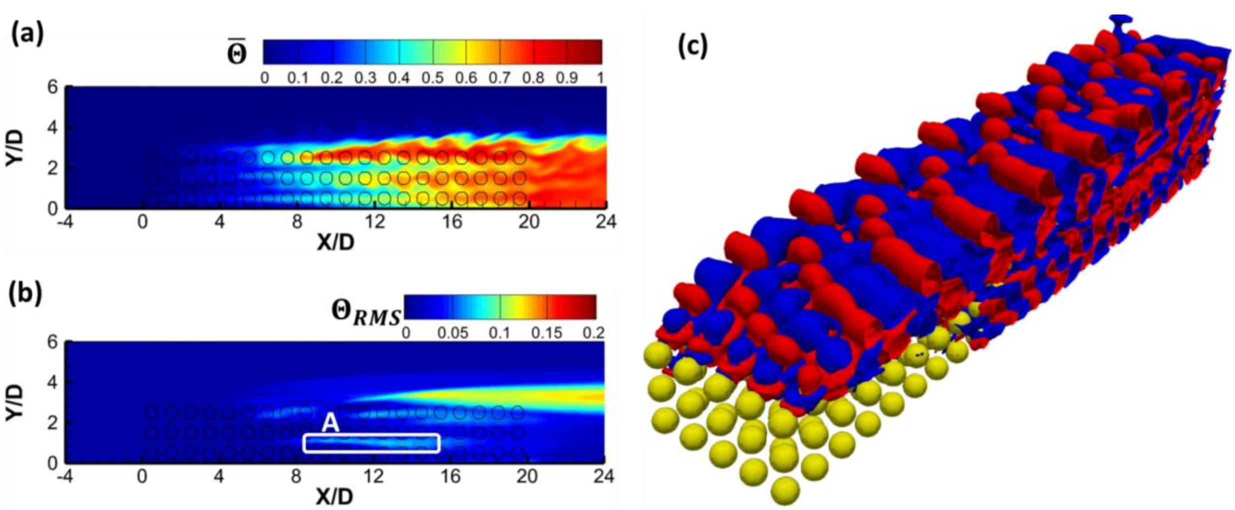

Figure 13 (a, b) Contour of non-dimensional instantaneous temperature ($\bar{\Theta}$) and temperature fluctuations (Θ_{RMS}), respectively, at Re = 3600 and high porosity (Φ = 91%); **(c)** Iso-surface of instantaneous vertical velocity fluctuations; **Blue**: negative value; **Red**: Positive value.

Figure 14(a-d) and (e-h) depict the vertical distribution of turbulent statistics for low- and high-porosity cases, respectively, at X/D = 1.5, 6.5 and 13.5. In **Figure 14**, $u^{*\prime}$ is defined as $u^{*\prime} = u'/U$ in the non-dimensional streamwise turbulent heat flux ($< \overline{u^{*\prime}\Theta'} >$). As shown in **Figure 14**(a-d), the vertical distributions of $< \overline{u^{*\prime}\Theta'} >$ and turbulent kinetic energy (TKE) are different in region#1 and #2. **Figure 14**(a, b) displays that in region#1 (X/D = 1.5 and 6.5), the maximum turbulence statistics occur away from the porous-fluid interface (marked as "R1"), as also can be seen in **Figure 12**(b). The spanwise distribution of turbulent heat flux at Re = 3600, previously discussed in **Figure 11**(b), confirms this trend, where the arc shape of maximum values in region#1 is located above the core of CRVPs, away from the interface. In **Figure 14**(a, b) at X/D = 13.5, belonging to region#2, the maximum turbulence statistics occur adjacent to the porous-fluid interface, marked by "R2". This is consistent with the previous findings in literature for fully-developed porous channel flow with periodic boundary conditions [19, 24, 29, 32]. Similar observations can be detected in **Figure 14**(c, d) at Re = 14400. However, it should be noted that the boundaries of regions#1 and #2 are different for Re = 14400 than those for Re = 3600. In fact, for Re = 14400 the transition from region#1 to region#2 occurs closer to the leading edge (see **Figure 4**). Hence, in **Figure 14**(c, d), the turbulence statistics at X/D = 6.5 and 13.5, located in region#2, experience a sharp gradient across the interface, marked by "R2". Finally, a comparison of turbulence statistics in **Figure 14**(a-d) indicates that inside the porous media, the turbulence fluctuations intensify beneath the interface as the Re number increases.

For high-porosity cases in **Figure 14**(e-h), the vertical distribution of turbulence statistics notifies two peaks inside the porous block (marked by "A" and "B") and one peak near the interface ("C"). It is seen that by increasing the Re number from 3600 to 14400, the elevation of peak values decreases. For example, for Re = 3600 at X/D = 13.5, the peaks are located at Y/D = 0.93, 2.57 and 3.32*,* while for Re = 14400, they are at Y/D = 0.75, 1.80 and 2.95, correspondingly. This means that, overall, they move toward the bottom wall by nearly 20%. Additionally, in **Figure 14**(g, h) at X/D = 13.5, the maximum values of turbulence statistics occur on the interface ("C"), similar to observations in **Figure 14**(c, d) at X/D = 13.5. Hence, regardless of porosity value, at higher Re numbers and far enough to the leading edge of the porous block (for example $X/D >$ 6.5), the turbulence statistics witness sharp gradient across the interface. Moreover, turbulence statistics for high-porosity cases are intensified inside the porous block by increasing the Re number, similar to the low-porosity cases. For instance, for Re = 3600, the mean value of TKE at X/D = 13.5 is 0.023, while it is almost doubled (~0.048) at Re = 14400 (see **Figure 14**(f, h)). A comparison of turbulence statistics between high- and low-porosity cases reveals higher turbulent fluctuations for low-porosity cases. For instance, at Re = 14400 and X/D = 13.5, the average TKE for high-porosity case is 0.022, while it increases to 0.035 for the low-porosity case.

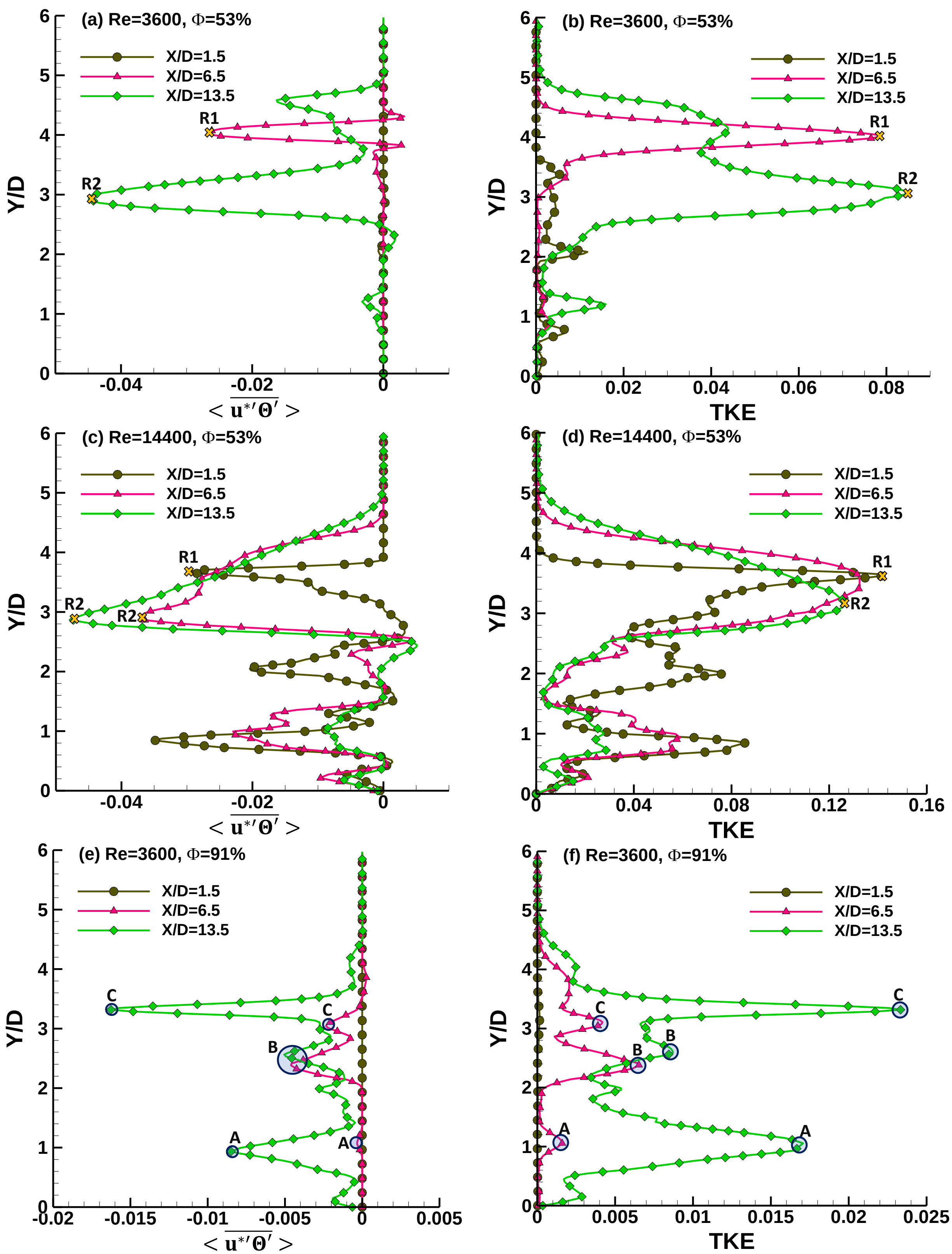
(a) Re=3600, Φ=53%
X/D=1.5
X/D=6.5
X/D=13.5
R1
R2
Y/D
< u*'Θ' >
(b) Re=3600, Φ=53%
X/D=1.5
X/D=6.5
X/D=13.5
R1
R2
Y/D
TKE
(c) Re=14400, Φ=53%
X/D=1.5
X/D=6.5
X/D=13.5
R1
R2
R2
Y/D
< u*'Θ' >
(d) Re=14400, Φ=53%
X/D=1.5
X/D=6.5
X/D=13.5
R1
R2
Y/D
TKE
(e) Re=3600, Φ=91%
X/D=1.5
X/D=6.5
X/D=13.5
A
A
B
C
C
Y/D
< u*'Θ' >
(f) Re=3600, Φ=91%
X/D=1.5
X/D=6.5
X/D=13.5
A
A
B
B
C
C
Y/D
TKE

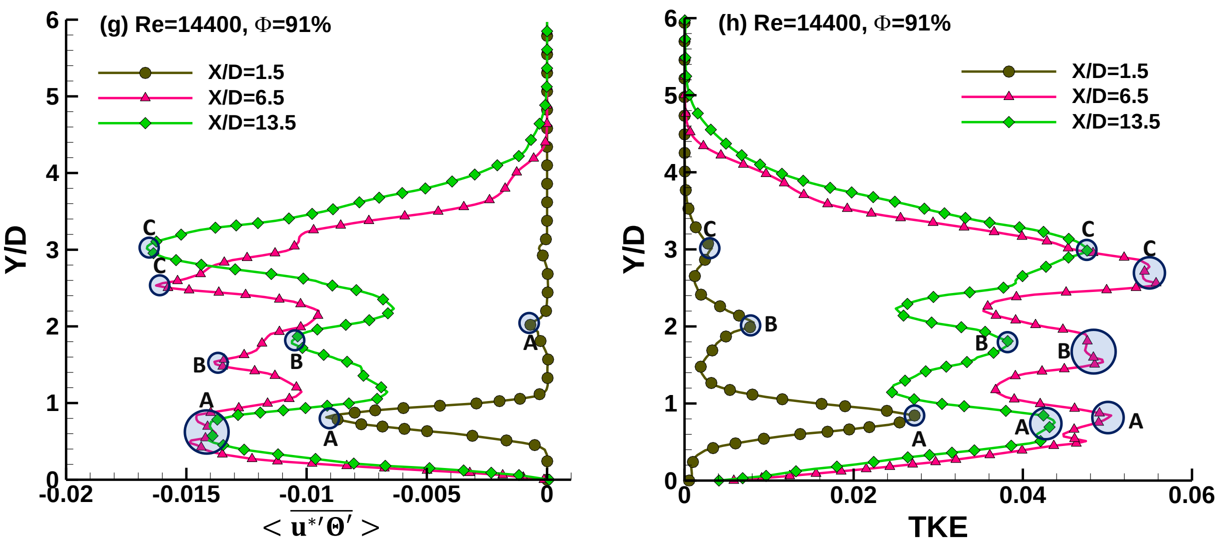

Figure 14 Vertical distribution of non-dimensional streamwise turbulent heat flux ($<\overline{u^{*\prime}\Theta^{\prime}}>$) and turbulent kinetic energy (TKE) at different locations (X/D = 1.5, 6.5 and 13.5) for Re = 3600 and 14400; **(a-d)** Low porosity; **(e-h)** High porosity.

Figure 15(a) shows a zoomed view of a single hairpin, coloured by streamwise vorticity. The hairpin legs and necks are characterised by high-/low-valued streamwise vorticities. The vortex line in **Figure 15**(a) demonstrates the rotation of the head, necks, and legs [31]. The stream vectors in **Figure 15**(a) represent the CRVPs and demonstrate how the high-momentum flow (vertical streamlines with positive velocity) leaks from the porous region into the non-porous region (flow leakage). **Figure 15**(b) depicts a single hairpin coloured by spanwise vorticity. The hairpin head is characterised by the clockwise rotation of velocity vectors and high-valued negative spanwise vorticity. The opposite direction of velocity vectors on the top and bottom of the hairpin head reveals a strong shear layer between the low-speed flow lump (over the interface) and accelerated flow above the hairpin (see **Figure 4**). The hairpins heads in region#1 and region#2 match with the maximum values of turbulence statistics, marked as “Max#1” and “Max#3”, respectively in **Figure 11** and **Figure 12**.

Figure 15(c) summarizes schematically the momentum and energy exchanges between the porous and non-porous regions in a composite porous-fluid system. The mutual turbulent interplay between the two regions is characterised by two major steps. In the first step, high-temperature fluid flow leaks from the porous region across the interface and penetrates the non-porous region. In this step, the energy and momentum exchanges between the porous region and low-speed flow lump are governed by CRVPs. Afterward, in the second step, the energy and momentum exchanges occur across the shear layer between the low-speed flow lump and low-temperature accelerated flow above the hairpins (see **Figure 4**). In this step, the flow induced by the clockwise rotation of the hairpin head leads to bottom-up and top-down turbulent interactions across the shear layer. For instance, by the top-down interaction, the low-temperature accelerated flow above the shear layer is driven down to the low-speed flow lump region.

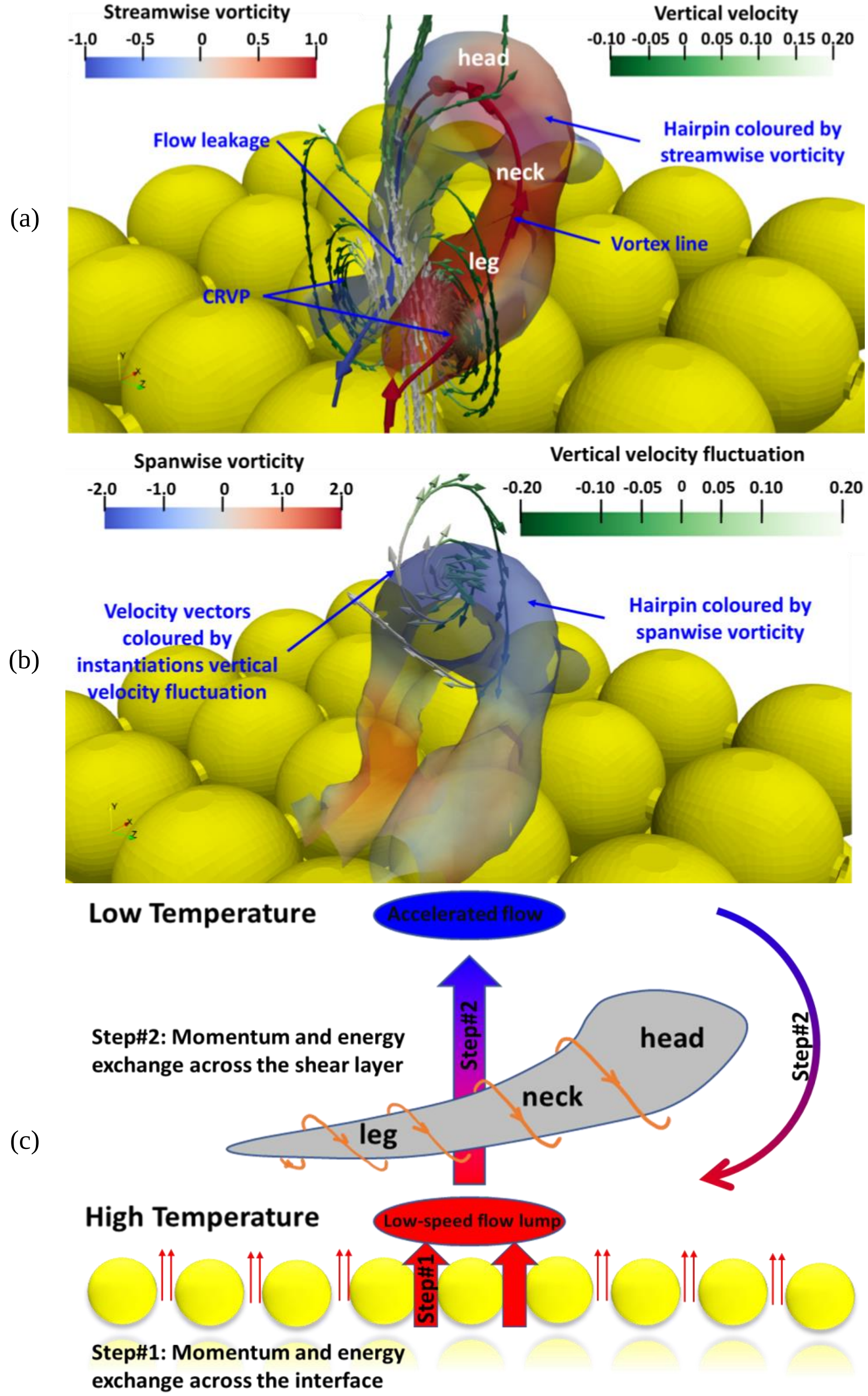

Figure 15 (a) Zoomed view of a single hairpin over the porous block, coloured by streamwise vorticity. Stream vectors coloured by vertical velocity represent CRVPs originating from porous inside; **(b)** Zoomed view of a single hairpin coloured by spanwise vorticity, and velocity vectors on the hairpin head which are coloured by instantaneous vertical velocity fluctuation; **(c)** Schematic representation of momentum and energy exchange mechanisms between porous and non-porous regions.

Figure 16 displays the contours of the time-averaged Nusselt (Nu) number on one slice of pore elements at the centre plane of the porous block. Comparing the low- and high-porosity cases reveals that at the same Re number, the higher Nu number belongs to the high-porosity case because of higher velocities inside the porous block. Overall, the Nu number experiences a significant reduction along the porous length from the leading to trailing edges, especially for low-porosity cases. In addition, **Figure 16** shows a non-uniform distribution for Nu number along the vertical direction for both porosities. For instance, in **Figure 16**(a), high-valued Nu number regions, marked as "A", are observed at the lower sides of the spheres due to the flow leakage from the porous region to the non-porous region. Besides, in **Figure 16**(a), some other high-valued Nu number areas, marked as "B", can be seen at both the lower and upper sides of pore elements located in the second and third rows of the porous block. These high Nu numbers correspond to the streamwise-oriented high-momentum paths in the horizontal direction inside the porous block, representing the channelling effect as shown in **Figure 4**(a).

Figure 16(b) displays that for high-porosity cases, regions with high Nu numbers are observed on both the upper and lower sides of the spheres with a symmetric pattern, marked as "C". The reason is that the incoming flow can easily penetrate through the gaps between the pore elements. In addition, the flow leakage for the high-porosity cases is significantly lower than that for the low-porosity cases. Therefore, maximum peaks of the Nu number marked as "C" in **Figure 16**(b) are caused mainly by high-momentum flow through the pores, regardless of the pores' elevation in the porous region.

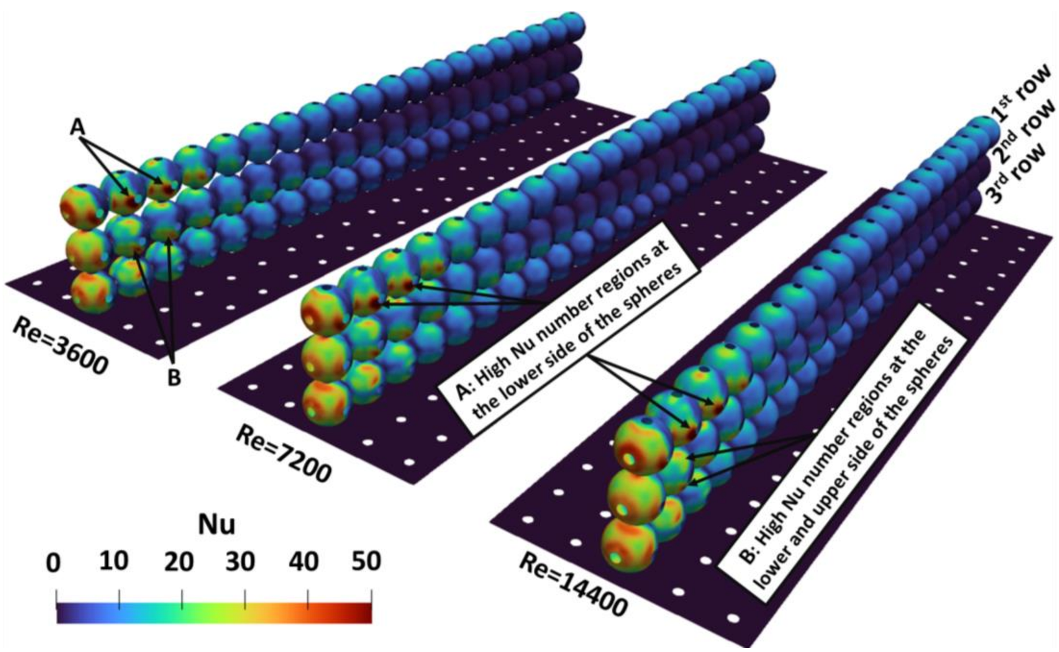

(a) Time-averaged Nusselt (Nu) number at three Re numbers and low porosity (Φ = 53%)

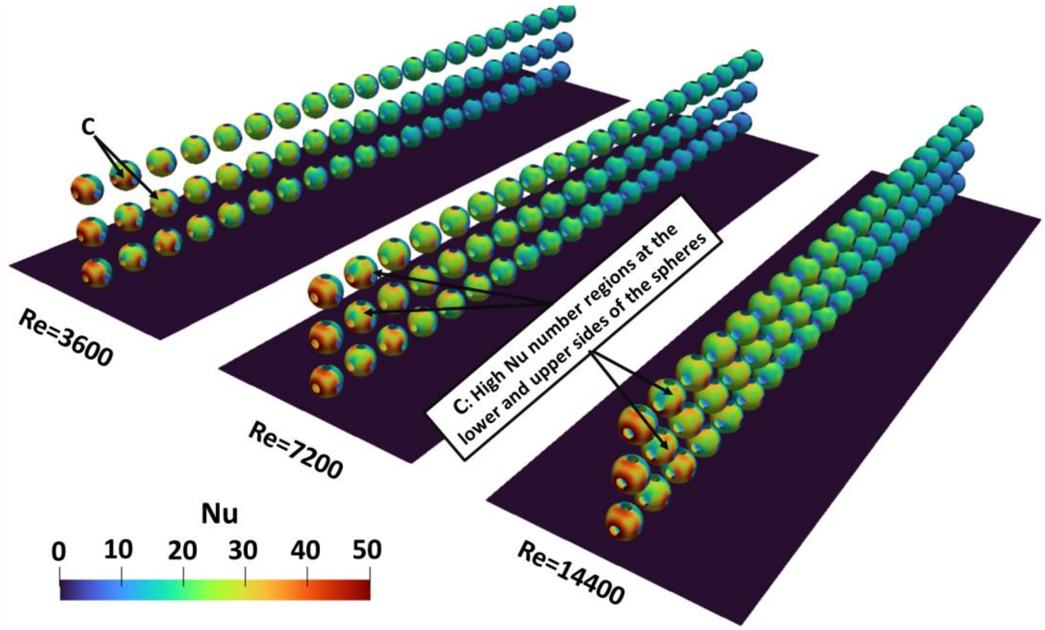

(b) Time-averaged Nusselt (Nu) number at three Re numbers and high porosity (Φ = 91%)

Figure 16 Time-averaged Nusselt (Nu) number ($Nu = \frac{D}{(k_f[T_{wall}-T_{inlet}]A_s)} \iint_{A_s} q_{wall,loc} dA_s$) distribution over pore elements at three Re numbers and two porosities; **(a)** Φ = 53%; **(b)** Φ = 91%.

Figure 17(a, b) displays the profiles of time-averaged Nu number and pressure drop along the porous length. **Figure 17**(a) demonstrates that the high-porosity cases yield higher Nu numbers compared to low-porosity cases. At the same Re number, the Nu number for the high-porosity case is at least 2.6 times higher than that of the low-porosity case. In addition, the effect of the Re number is almost the same for both low-porosity and high-porosity cases. In fact, as the Re number increases from 3600 to 14400, the overall Nu number raises by ~3.6 times and ~3.2 times for the low-porosity and high-porosity cases, respectively. Generally, by moving downstream, the Nu number reduction for low-porosity cases is more than that for the high-porosity cases. The maximum Nu reduction is observed for the low-porosity case at Re = 3600, where the Nu number at the leading edge is about 23.7 times higher than that at the trailing edge. In contrast, the minimum Nu reduction is observed for the high-porosity case at Re = 14400, for which the Nu number at the leading edge is about three times higher than that at the trailing edge. When the Re number increases from 3600 to 14400, the ratio of the Nu number at the leading edge to that at the trailing edge drops from 23.7 to 9.4 for low-porosity cases. However, this ratio reduces from 6.7 to 3.1 by increasing the Re number for high-porosity cases. The conclusion is that porous elements of high-porosity cases are more likely to exchange energy than those of low-porosity cases through the entire porous length.

In **Figure 17**(b), the pressure drop is calculated by the difference between the pressure at the reference point ($P_{ref@X/D=0}$) and pressure at a specific location ($P_{@X/D}$). **Figure 17**(b) demonstrates that along the porous length, the maximum pressure drop is for the low-porosity case with Re = 14400, and the minimum pressure loss is for the high-porosity case with Re = 3600. Also, at the same Re number, the lower the porosity, the higher the pressure drop, and at the same porosity, the higher the Re number, the greater the pressure drop. The results show that regardless of the Re number, the pressure drop near the leading edge for the low-porosity case is about 3.5 times greater than that for the high-porosity case. Higher pressure drop for the low-porosity case demonstrates the strong blocking effect to allow a flow penetration through the porous block, resulting in flow separation near the leading edge. The overall pressure drop for the low-porosity case is about 1.8 times higher than that for the high-porosity case, regardless of the Re number. Furthermore, for both porosities, with an increase in Re number from 3600 to 14400, the pressure drop through the entire porous length increases by ~14 times. Comparing **Figure 17**(a) and **Figure 17**(b) shows that for a fixed Re

number, the porous structure with higher porosity yields a higher Nu number at a lower pressure drop.

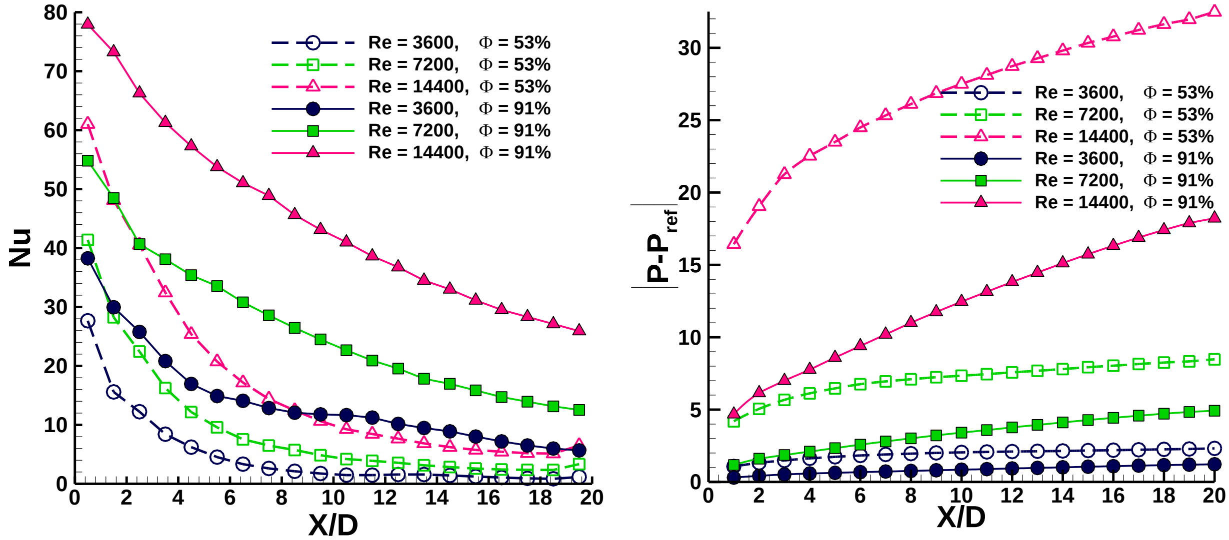

(a) Distribution of Nu number along the porous block

(b) Distribution of pressure drop along the porous block

Figure 17 Distribution of Nu number and pressure drop along the porous length at three different Re numbers and two porosities: 53% and 91%.

4 Conclusions

Pore-scale large eddy simulations (LES) are performed for composite porous-fluid systems with two different porosities (53% and 91%) at three Re numbers (3600, 7200, and 14400). The major objective of the present study was to fill the gap in the literature regarding the effect of the porosity and Re number on the different mechanisms of momentum and energy exchanges across the porous-fluid interface in composite porous-fluid systems with a finite length. In addition, this paper tried to answer the challenging question about the validity of earlier findings in the fully-developed porous channel flows [24, 25, 28, 29, 32]. To this end, as opposed to the fully-developed porous channel flows, a finite porous block (LR = 20) immersed in a turbulent channel flow is investigated, where the boundary layer separation and reattachment occur. The key findings of the present paper are as follows:

1) The generation of hairpin structures over the porous block controls the momentum and energy exchanges in two steps: Firstly, the mutual turbulent interplay near the interface which is governed by hairpin legs; Secondly, the bottom-up and top-down turbulent interactions far away from the interface across the shear layer which are the result of induced flow by the clockwise rotation of the hairpin heads. Temporal and spatial analysis of coherent structures revealed that the evolution of hairpin structures is affected by Re number and porosity.
2) Increasing porosity reduces flow leakage up to 50% which disorders the counter-rotating vortex pairs (CRVPs') patterns and consequently hairpin structures. Further, the effect of the Re number on the flow leakage is more pronounced for low-porosity cases. The results showed that by increasing the Re number from 3600 to 14400, the flow leakage declines nearly 10% for low-porosity cases, however, it drops about 5% for high-porosity cases.
3) For low-porosity cases, regardless of the Re number, two distinct regions are detected over the interface. Region#1 with organised hairpin structures is characterised by a high flow leakage and the formation of a turbulent separation bubble (TSB). Region#2 with unorganised hairpin structures is characterised by lower flow leakage, reattachment of the separated flow, and redevelopment of the boundary layer. Increasing the Re number shortens the length of region#1. For high-porosity

cases, containing disordered hairpin structures, two distinct regions are not identified at any Re number owing to the absence of flow separation at the leading edge and negligible flow leakage.

4) In region#1, maximum turbulent fluctuations occur far away from the interface, while they approach the interface in region#2. JPDFs of velocity fluctuations showed that momentum is exchanged in region#1 by inward/outward intersection events. Whereas, in region#2, the streamwise and vertical velocity fluctuations are anti-correlated, and sweep/ejection event is the dominant mechanism.
5) The location of maximum turbulence statistics approaches the interface by increasing the Re number or porous length. It supports earlier literature findings for a fully-developed porous channel flow [19, 24, 25, 29, 32], which emphasizes the turbulent interaction at the interface. Therefore, the previous literature findings only apply to region#2. However, when the Re number is low or the porous length is short (LR = 10), the turbulent interplay between porous and non-porous regions is mainly controlled by the TSB and flow leakage. This observation is confirmed by the flow features in region#1, and recent findings of current authors in [30, 31], where LR = 10.
6) At the same Re number, the Nu number of the high-porosity case is at least 2.6 times greater than that of the low-porosity case. For low-porosity cases, the Nu number decreases more along the porous length. For instance, the Nu number ratio at the leading edge to the trailing edge is nearly 9.4 for the low-porosity case at Re = 14400. In contrast, it is only 3.1 in the high-porosity case. Finally, regardless of the Re number, the low-porosity case has 1.8 times more pressure drop than the high-porosity case.

Supplementary research in different directions has been left open for future studies. Some of the future research directions are outlined as follows:

1) In the present study, the temperature of the pore elements was considered constant with the Dirichlet boundary condition. For future studies, the solid part of pore elements could be added to the computational domain to investigate the heat transfer characteristics between fluid and solid parts more accurately by implementing conjugate heat transfer modelling.
2) The computational domain in this study consisted of finite porous blocks characterized by BR = 0.5, AR = 6.6, and LR = 20 with different porosities. The effects of blockage ratio (BR) and aspect ratio (AR) on the characteristics of regions #1 and #2 can be investigated in future studies using porous bluff bodies with varying BRs and ARs.
3) The inflow boundary condition in this study was a constant velocity profile with a constant temperature. For future studies, time-dependent inlet profiles can be implemented to investigate the flow physics of a composite porous-fluid system under transient conditions.
4) The porous block in this study is a cubic arrangement of uniform spheres. For a more realistic prediction of flow and thermal features in industrial applications, a randomly packed bed needs to be investigated to identify the influence of packed bed randomness on the physics of flow leakage, channelling effect and wake flow.

Acknowledgement

This work was supported by the UK Engineering and Physical Sciences Research Council (EPSRC) [grant numbers EP/W033542/1 and EP/T012242/2]. Data supporting this publication can be obtained on request. The authors would like to acknowledge the assistance given by Research IT and the use of the Computational Shared Facility at The University of Manchester.

References

[1] K. Duan *et al.*, "Multiphase and pore scale modeling on catalyst layer of high-temperature polymer electrolyte membrane fuel cell," *Journal of The Electrochemical Society*, vol. 168, no. 5, p. 054521, 2021.

[2] O. Yasar, E. Ozbek, S. Ekici, E. Yalcin, A. Midilli, and T. H. Karakoc, "Assessment of fuel cell studies with particle image velocimetry applications: A key review," *International Journal of Hydrogen Energy*, vol. 46, no. 57, pp. 29568-29582, 2021.

[3] Y. Mahmoudi, K. Hooman, and K. Vafai, *Convective Heat Transfer in Porous Media*. , 1st ed., CRC Press, Boca Raton, 2019.

[4] M. Khaljani, M. Nazari, M. Azarpeyvand, and Y. Mahmoudi, "Experimental and Pore-Scale Analysis of Flow and Thermal Fields in a Packed Bed Channel," *Heat Transfer Engineering*, vol. 43, no. 13, pp. 1119-1134, 2022.

[5] H. Torab and D. E. Beasley, "Optimization of a Packed Bed Thermal Energy Storage Unit," *Journal of Solar Energy Engineering*, vol. 109, no. 3, pp. 170-175, 1987.

[6] A. Gautam and R. Saini, "A review on technical, applications and economic aspect of packed bed solar thermal energy storage system," *Journal of Energy Storage*, vol. 27, p. 101046, 2020.

[7] M. Jadidi, H. K. Param, A. Revell, and Y. Mahmoudi, "Large eddy simulations of turbulent heat transfer in packed bed energy storage systems," *Journal of Energy Storage*, vol. 59, p. 106449, 2023.

[8] E. Barbour, D. Mignard, Y. Ding, and Y. Li, "Adiabatic compressed air energy storage with packed bed thermal energy storage," *Applied Energy*, vol. 155, pp. 804-815, 2015.

[9] Y. Deng *et al.*, "Effects of different coolants and cooling strategies on the cooling performance of the power lithium ion battery system: A review," *Applied Thermal Engineering*, vol. 142, pp. 10-29, 2018.

[10] G. Xia, L. Cao, and G. Bi, "A review on battery thermal management in electric vehicle application," *Journal of Power Sources*, vol. 367, pp. 90-105, 2017.

[11] Y. Wang, Y. Yu, Z. Jing, C. Wang, G. Zhou, and W. Zhao, "Thermal performance of lithium-ion batteries applying forced air cooling with an improved aluminium foam heat sink design," *International Journal of Heat and Mass Transfer*, vol. 167, p. 120827, 2021.

[12] Z. Nie, Y. Lin, and Q. Tong, "Numerical simulations of two-phase flow in open-cell metal foams with application to aero-engine separators," *International Journal of Heat and Mass Transfer*, vol. 127, pp. 917-932, 2018.

[13] G.-W. Chu, L. Sang, X.-K. Du, Y. Luo, H.-K. Zou, and J.-F. Chen, "Studies of CO2 absorption and effective interfacial area in a two-stage rotating packed bed with nickel foam packing," *Chemical Engineering and Processing: Process Intensification*, vol. 90, pp. 34-40, 2015.

[14] H. Zhang, Z. Zou, L. Qi, and H. Liu, "Investigation of metallic foam in the application of turbine cooling," *Procedia Engineering*, vol. 27, pp. 752-761, 2012.

[15] G. K. Marri and C. Balaji, "Experimental and numerical investigations on the effect of porosity and PPI gradients of metal foams on the thermal performance of a composite phase change material heat sink," *International Journal of Heat and Mass Transfer*, vol. 164, p. 120454, 2021.

[16] R. Singh, A. Akbarzadeh, and M. Mochizuki, "Sintered porous heat sink for cooling of high-powered microprocessors for server applications," *International Journal of Heat and Mass Transfer*, vol. 52, no. 9-10, pp. 2289-2299, 2009.

[17] A. Saez and B. McCoy, "Dynamic response of a packed bed thermal storage system—a model for solar air heating," *Solar Energy*, vol. 29, no. 3, pp. 201-206, 1982.

[18] R. Domański and G. Fellah, "Thermoeconomic analysis of sensible heat, thermal energy storage systems," *Applied Thermal Engineering*, vol. 18, no. 8, pp. 693-704, 1998.

[19] W. Breugem, B. Boersma, and R. Uittenbogaard, "The influence of wall permeability on turbulent channel flow," *Journal of Fluid Mechanics*, vol. 562, pp. 35-72, 2006.

[20] M. Ghosh and R. Das, "Influence of Form-Induced Shear Stress on Turbulent Kinetic Energy Budget Distributions Above and Within the Flow-Gravel-Bed Interface in Permeable Gravel Bed Stream—a Comparative Study," *Water Resources*, vol. 48, no. 4, pp. 544-556, 2021.

[21] X. Chu, W. Wang, G. Yang, A. Terzis, R. Helmig, and B. Weigand, "Transport of turbulence across permeable interface in a turbulent channel flow: interface-resolved direct numerical simulation," *Transport in Porous Media*, vol. 136, no. 1, pp. 165-189, 2021.

[22] Y. Mahmoudi and N. Karimi, "Numerical investigation of heat transfer enhancement in a pipe partially filled with a porous material under local thermal non-equilibrium condition," *International Journal of Heat and Mass Transfer*, vol. 68, pp. 161-173, 2014.

[23] T. Kim, G. Blois, J. L. Best, and K. T. Christensen, "Experimental study of turbulent flow over and within cubically packed walls of spheres: Effects of topography, permeability and wall thickness," *International Journal of Heat and Fluid Flow*, vol. 73, pp. 16-29, 2018.

[24] K. Suga, Y. Matsumura, Y. Ashitaka, S. Tominaga, and M. Kaneda, "Effects of wall permeability on turbulence," *International Journal of Heat and Fluid Flow*, vol. 31, no. 6, pp. 974-984, 2010.

[25] C. Manes, D. Pokrajac, I. McEwan, and V. Nikora, "Turbulence structure of open channel flows over permeable and impermeable beds: A comparative study," *Physics of Fluids*, vol. 21, no. 12, p. 125109, 2009.

[26] C. Manes, D. Poggi, and L. Ridolfi, "Turbulent boundary layers over permeable walls: scaling and near-wall structure," *Journal of Fluid Mechanics*, vol. 687, pp. 141-170, 2011.

[27] Y. Kuwata and K. Suga, "Transport mechanism of interface turbulence over porous and rough walls," *Flow, Turbulence and Combustion*, vol. 97, no. 4, pp. 1071-1093, 2016.

[28] K. Suga, Y. Okazaki, and Y. Kuwata, "Characteristics of turbulent square duct flows over porous media," *Journal of Fluid Mechanics*, vol. 884, 2020.

[29] K. Suga, M. Mori, and M. Kaneda, "Vortex structure of turbulence over permeable walls," *International Journal of Heat and Fluid Flow*, vol. 32, no. 3, pp. 586-595, 2011.

[30] M. Jadidi, A. Revell, and Y. Mahmoudi, "Pore-scale Large Eddy Simulation of Turbulent Flow and Heat Transfer over Porous Media," *Applied Thermal Engineering*, p. 118916, 2022.

[31] M. Jadidi, H. K. Param, A. Revell, and Y. Mahmoudi, "Flow leakage and Kelvin–Helmholtz instability of turbulent flow over porous media," *Physics of Fluids*, vol. 34, no. 10, p. 105114, 2022.

[32] K. Suga, "Understanding and modelling turbulence over and inside porous media," *Flow, Turbulence and Combustion*, vol. 96, no. 3, pp. 717-756, 2016.

[33] F. S. Anuar, I. A. Abdi, and K. Hooman, "Flow visualization study of partially filled channel with aluminium foam block," *International Journal of Heat and Mass Transfer*, vol. 127, pp. 1197-1211, 2018.

[34] F. S. Anuar, I. A. Abdi, M. Odabaee, and K. Hooman, "Experimental study of fluid flow behaviour and pressure drop in channels partially filled with metal foams," *Experimental Thermal and Fluid Science*, vol. 99, pp. 117-128, 2018.

[35] J.-M. Leu, H.-C. Chan, and M. Chu, "Comparison of turbulent flow over solid and porous structures mounted on the bottom of a rectangular channel," *Flow Measurement and Instrumentation*, vol. 19, no. 6, pp. 331-337, 2008.

[36] F. S. Anuar, K. Hooman, M. R. Malayeri, and I. A. Abdi, "Experimental study of particulate fouling in partially filled channel with open-cell metal foam," *Experimental Thermal and Fluid Science,* vol. 110, p. 109941, 2020.

[37] W. Wang, X. Chu, A. Lozano-Durán, R. Helmig, and B. Weigand, "Information transfer between turbulent boundary layers and porous media," *Journal of Fluid Mechanics,* vol. 920, 2021.

[38] R. Habib, N. Karimi, B. Yadollahi, M. H. Doranehgard, and L. K. Li, "A pore-scale assessment of the dynamic response of forced convection in porous media to inlet flow modulations," *International Journal of Heat and Mass Transfer,* vol. 153, p. 119657, 2020.

[39] J. Linsong, W. Ping, and F. Antonio, "Multi-scale simulation of turbulence and heat transfer characteristics in randomly packed beds," *Powder Technology,* vol. 377, pp. 29-40, 2021.

[40] P. Poureslami, M. Siavashi, H. Moghimi, and M. Hosseini, "Pore-scale convection-conduction heat transfer and fluid flow in open-cell metal foams: A three-dimensional multiple-relaxation time lattice Boltzmann (MRT-LBM) solution," *International Communications in Heat and Mass Transfer,* vol. 126, p. 105465, 2021.

[41] H. Moghimi, M. Siavashi, M. M. Nezhad, and A. Guadagnini, "Pore-scale computational analyses of non-Darcy flow through highly porous structures with various degrees of geometrical complexity," *Sustainable Energy Technologies and Assessments,* vol. 52, p. 102048, 2022.

[42] E. Sepehri and M. Siavashi, "Pore-scale direct numerical simulation of fluid dynamics, conduction and convection heat transfer in open-cell Voronoi porous foams," *International Communications in Heat and Mass Transfer,* vol. 137, p. 106274, 2022.

[43] D. Korba and L. Li, "Effects of pore scale and conjugate heat transfer on thermal convection in porous media," *Journal of Fluid Mechanics,* vol. 944, 2022.

[44] A. G. Dixon, M. Nijemeisland, and E. H. Stitt, "Systematic mesh development for 3D CFD simulation of fixed beds: Contact points study," *Computers & Chemical Engineering,* vol. 48, pp. 135-153, 2013.

[45] S. B. Pope and S. B. Pope, *Turbulent Flows*. Cambridge university press, 2000.

[46] P. Sagaut, *Large Eddy Simulation for Incompressible Flows: An Introduction*. Springer Science & Business Media, 2006.

[47] W.-W. Kim, S. Menon, W.-W. Kim, and S. Menon, "Application of the localized dynamic subgrid-scale model to turbulent wall-bounded flows," in *35th Aerospace Sciences Meeting and Exhibit,* 1997, p. 210.

[48] W. M. Kays, "Turbulent Prandtl number. Where are we?," *ASME Journal of Heat Transfer,* vol. 116, no. 2, pp. 284-295, 1994.

[49] H. Jasak, A. Jemcov, and Z. Tukovic, "OpenFOAM: A C++ library for complex physics simulations," in *International workshop on coupled methods in numerical dynamics*, 2007, vol. 1000: IUC Dubrovnik Croatia, pp. 1-20.

[50] F. Bazdidi-Tehrani, A. Ghafouri, and M. Jadidi, "Grid resolution assessment in large eddy simulation of dispersion around an isolated cubic building," *Journal of Wind Engineering and Industrial Aerodynamics*, vol. 121, pp. 1-15, 2013.

[51] I. Celik, M. Klein, and J. Janicka, "Assessment measures for engineering LES applications," *Journal of Fluids Engineering,* vol. 131, no. 3, 2009.

[52] L. Davidson, "How to estimate the resolution of an LES of recirculating flow," in *Quality and Reliability of Large-Eddy Simulations II*: Springer, 2011, pp. 269-286.

[53] S. B. Pope, "Ten questions concerning the large-eddy simulation of turbulent flows," *New Journal of Physics*, vol. 6, no. 1, p. 35, 2004.

[54] I. B. Celik, Z. N. Cehreli, and I. Yavuz, "Index of Resolution Quality for Large Eddy Simulations," *Journal of Fluids Engineering,* vol. 127, no. 5, pp. 949-958, 2005.

[55] S. Ergun, "Fluid flow through packed columns," *Chemical Engineering Progress*, vol. 48, pp. 89-94, 1952.

[56] K. Vafai, W. Minkowycz, A. Bejan, K. Khanafer, and E. Sparrow, "Synthesis of models for turbulent transport through porous media," *Handbook of Numerical Heat Transfer,* 2006.

[57] R.B. Bird, W.E. Stewart, E.N. Lightfoot, Transport Phenomena, 1st ed., John Wiley & Sons, New York, 1960.

[58] W.M. Kays, A.L. London, Compact Heat Exchangers., 3th ed., McGraw-Hill, New York,1984.

[59] T. L. Bergman, A. S. Lavine, F. P. Incropera, and D. P. DeWitt, *Introduction to Heat Transfer*. John Wiley & Sons, 2011.

[60] F. Kuwahara, M. Shirota, and A. Nakayama, "A numerical study of interfacial convective heat transfer coefficient in two-energy equation model for convection in porous media," *International Journal of Heat and Mass Transfer,* vol. 44, no. 6, pp. 1153-1159, 2001.

[61] X. Nie, R. Evitts, R. Besant, and J. Bolster, "A new technique to determine convection coefficients with flow through particle beds," *Journal of Heat Transfer*, vol. 133, no. 4, 2011.

[62] M. Nazari, D. Jalali Vahid, R. K. Saray, and Y. Mahmoudi, "Experimental investigation of heat transfer and second law analysis in a pebble bed channel with internal heat generation," *International Journal of Heat and Mass Transfer*, vol. 114, pp. 688-702, 2017.

[63] J. S. Lee and K. Ogawa, "Pressure Drop Though Packed Bed," *Journal of Chemical Engineering of Japan*, vol. 27, no. 5, pp. 691-693, 1994.

[64] S. S. Lu and W. W. Willmarth, "Measurements of the structure of the Reynolds stress in a turbulent boundary layer," *Journal of Fluid Mechanics,* vol. 60, no. 3, pp. 481-511, 1973.

[65] W. K. George, "Lectures in Turbulence for the 21st Century," *Chalmers University of Technology,* vol. 550, 2013.

[66] T. Kim, G. Blois, J. L. Best, and K. T. Christensen, "Experimental evidence of amplitude modulation in permeable-wall turbulence," *Journal of Fluid Mechanics,* vol. 887, 2020.